iScience

CellPress
OPEN ACCESS

Article

Induced retinal pigment epithelial cells with anti-epithelial-to-mesenchymal transition ability delay retinal degeneration

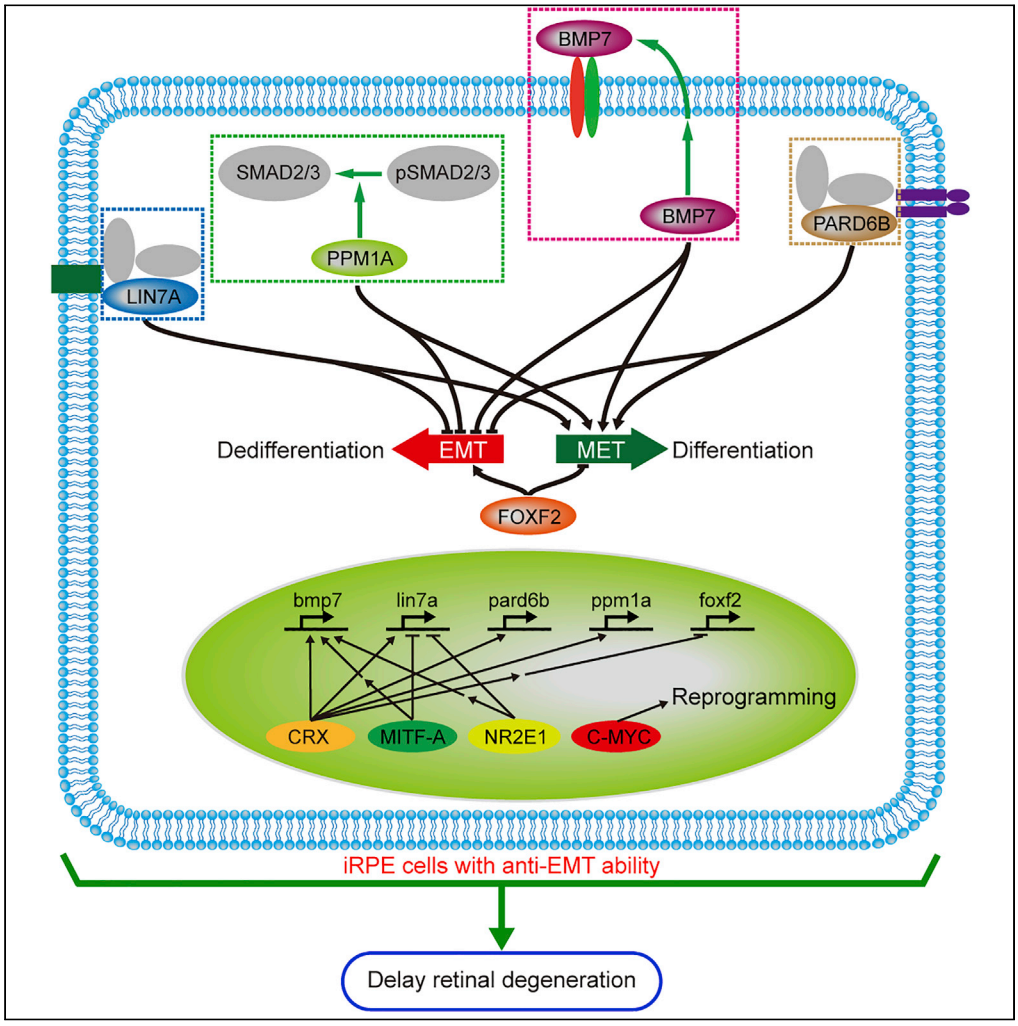

Haibin Tian, Zhiyang Chen, Xiaoman Zhu, ..., Jieping Zhang, Lixia Lu, Guo-Tong Xu

tianhb@tongji.edu.cn (H.T.)
lulixia@tongji.edu.cn (L.L.)
gtxu@tongji.edu.cn (G.-T.X.)

Highlights

CRX, MITF-A, NR2E1, and C-MYC transform De-iPSC-RPE cells into iRPE cells

iRPE cells have resistance to TGF-β-induced EMT

BMP7, FOXF2, LIN7A, PARD6B, and PPM1A mediate the functions of TFs in iRPE cells

iRPE cells have better retinal protective function than iPSC-RPE cells

Tian et al., iScience 25, 105050
October 21, 2022
https://doi.org/10.1016/j.isci.2022.105050

iScience

CellPress
OPEN ACCESS

Article

Induced retinal pigment epithelial cells with anti-epithelial-to-mesenchymal transition ability delay retinal degeneration

Haibin Tian,[1,5,6,*] Zhiyang Chen,[1,5] Xiaoman Zhu,[1,5] Qingjian Ou,[1] Zhe Wang,[1] Binxin Wu,[1] Jing-Ying Xu,[1] Caixia Jin,[1] Furong Gao,[1] Juan Wang,[1] Jingfa Zhang,[2] Jieping Zhang,[1] Lixia Lu,[1,*] and Guo-Tong Xu[1,3,4,*]

SUMMARY

The hostile microenvironment of the retina in patients with age-related macular degeneration (AMD) may trigger epithelial-to-mesenchymal transition (EMT) of grafted retinal pigment epithelial (RPE) cells, thus attenuating the therapeutic outcome. Here, we transformed human dedifferentiated induced pluripotent stem cell-derived RPE (iPSC-RPE) cells into induced RPE (iRPE) cells using a cocktail of four transcription factors (TFs)—CRX, MITF-A, NR2E1, and C-MYC. These critical TFs maintained the epithelial property of iRPE cells by regulating the expression of *bmp7*, forkhead box f2, *lin7a*, and *pard6b*, and conferred resistance to TGF-β-induced EMT in iRPE cells by targeting *ppm1a*. The iRPE cells with Tet-on system-regulated *c-myc* expression exhibited EMT resistance and better therapeutic function compared with iPSC-RPE cells in rat AMD model. Our study demonstrates that endowing RPE cells with anti-EMT property avoids the risk of EMT after cells are grafted into the subretinal space, and it may provide a suitable candidate for AMD treatment.

INTRODUCTION

Age-related macular degeneration (AMD) has two subtypes, dry AMD and wet AMD, and is the leading cause of visual impairment worldwide (Hadziahmetovic and Malek, 2020; Ruan et al., 2021). Dysfunction of RPE cells is thought to be the primary pathogenic process of AMD. To date, no efficient therapeutic strategies have been developed (Hadziahmetovic and Malek, 2020). Although a revolutionary anti-vascular endothelial growth factor (VEGF) therapy has been developed to treat wet AMD, co-occurrence of geographic atrophy is the main complication of this therapeutic strategy, thus deterring its long-term use (Grunwald et al., 2014). Hence, a logical approach to mitigate AMD is to replace dysfunctional RPE cells by transplanting healthy RPE cells (Alexander et al., 2015).

Early preclinical experiments and clinical trials used adult or fetal RPE cells to treat AMD (Binder et al., 2002; Peyman et al., 1991; van Romunde et al., 2015). However, healthy RPE cells cannot be easily obtained, and invasive surgical procedures and/or ethical concerns limit the use of autologous or allogenic RPE cells. Recently, human embryonic stem cell-derived RPE (hESC-RPE) cells and induced pluripotent stem cell-derived RPE (iPSC-RPE) cells have been used in clinical trials and favorable outcomes have been achieved through cell transplantation (da Cruz et al., 2018; Liu et al., 2018; Mandai et al., 2017; Mehat et al., 2018; Schwartz et al., 2015; Song et al., 2015; Sugita et al., 2020; Sung et al., 2021; Takagi et al., 2019).

There are two main approaches to RPE cell transplantation: Grafting of the RPE cell suspension or delivery of a monolayer of RPE cells into the subretinal space. However, subretinal space is a hostile microenvironment; increased levels of transforming growth factor (TGF)-β, an inducer of epithelial-to-mesenchymal transition (EMT), have been confirmed in the retina of patients with AMD (Amin et al., 1994; Reddy et al., 1995). Previous studies have demonstrated that part of RPE cells from post-mortem human eyes with AMD undergo EMT by positive staining with EMT markers (Ghosh et al., 2018; Hirasawa et al., 2011). As a result, the transplanted RPE cells might be at a risk of EMT induction *in vivo* and subsequently weaken the therapeutic outcome. In addition, previous studies reported that part of grafted RPE cell may leak into the vitreous cavity to participate in the formation of an epiretinal membrane (ERM) (Mehat et al., 2018; Song et al., 2015), and ERM formation is able to weaken stem cell-based therapeutic outcomes in

[1]Department of Ophthalmology of Tongji Hospital and Laboratory of Clinical and Visual Sciences of Tongji Eye Institute, Tongji University School of Medicine, Shanghai 200065, China

[2]Department of Ophthalmology, Shanghai General Hospital (Shanghai First People's Hospital), Shanghai Jiao Tong University, Shanghai 200080, China

[3]Department of Physiology and Pharmacology, Tongji University School of Medicine, Shanghai 200092, China

[4]The collaborative Innovation Center for Brain Science, Tongji University, Shanghai 200092, China

[5]These authors contributed equally

[6]Lead contact

*Correspondence: tianhb@tongji.edu.cn (H.T.), lulixia@tongji.edu.cn (L.L.), gtxu@tongji.edu.cn (G.-T.X.)

https://doi.org/10.1016/j.isci.2022.105050

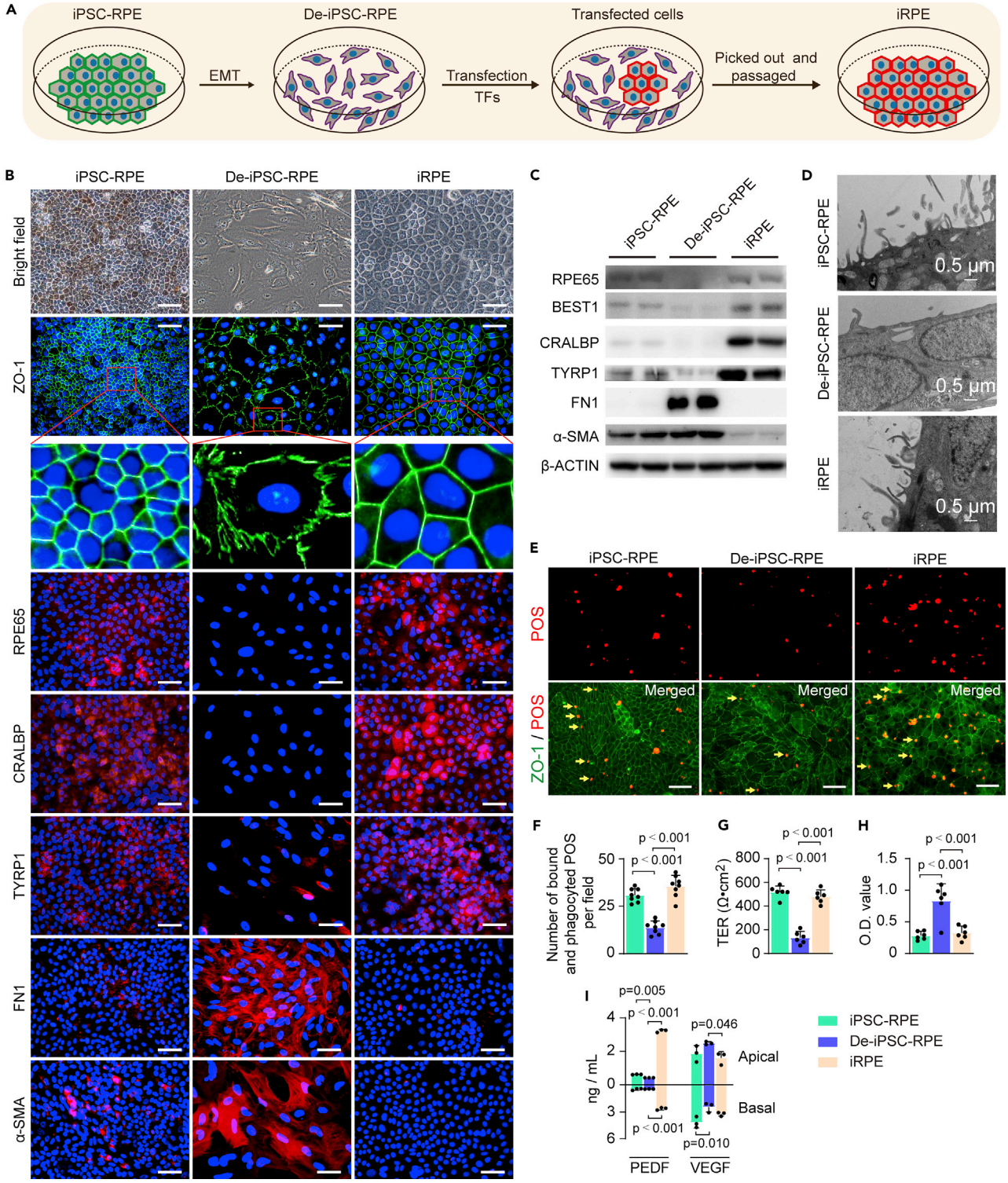

Figure 1. iRPE cells have similar phenotype and functions as iPSC-RPE cells

(A) Schematic for the transforming process. A cocktail of TF-expressing retroviruses was used to transfect De-iPSC-RPE cells. After seven days, iRPE clone was observed in the culture and picked out for subculturing.

(B and C) RPE-specific and EMT-associated markers detected by (B) immunostaining and (C) western blotting after cells were cultured for 8 days. The expression pattern of these markers in iRPE cells is more similar to that in iPSC-RPE cells. Scale bar = 50 μm.

Figure 1. *Continued*

(D) Electron micrographs of iPSC-RPE cells, De-iPSC-RPE cells, and iRPE cells demonstrated that quite a few microvilli were on the surface of iRPE and iPSC-RPE cells. Scale bar = 0.5 μm.

(E and F) The bound and phagocyted POSs (pointed by arrows) in iPSC-RPE, De-iPSC-RPE, and iRPE cells (E) and quantification of phagocytosis (F) as determined by the number of bound and phagocyted POS per field. Scale bar = 50 μm. Data are mean ± SD, one-way ANOVA and post hoc Bonferroni test, $n \geq 5$.

(G and H) TER analysis (G) and HRP permeability assay (H) showed that iRPE cells maintained the same epithelial integrity as iPSC-RPE cells. Data are mean ± SD, one-way ANOVA and post hoc Bonferroni test, n = 6.

(I) Expression levels of PEDF and VEGF from upper and lower chambers were determined by ELISA. iRPE cells and iPSC-RPE cells demonstrated similar secretion patterns. Data are mean ± SD, one-way ANOVA and post hoc Bonferroni test, n = 3.

AMD (Hu et al., 2020; Hussain et al., 2019; Kuriyan et al., 2017). Therefore, the generation of RPE cells that possess anti-EMT function and inhibit ERM formation might improve the efficacy of RPE cell treatment for AMD.

A group of studies have delineated several culture systems and factors that efficiently inhibit EMT in RPE cells or induce mesenchymal-to-epithelial transition (MET) in dedifferentiated RPE cells *in vitro*; these culture systems and factors include the Ca2+-switch protocol (Rak et al., 2006), TGF-β and notch receptor inhibitors, and retinoic acid receptor-γ agonist (Chen et al., 2014; Kimura et al., 2015; Nassar et al., 2014). However, it is difficult to apply these *in vitro* culture conditions in an *in vivo* microenvironment. An increasing number of studies have reported the direct transformation of cells from one lineage to another by key transcription factors (TFs) (D'Alessio et al., 2015; Shih et al., 2017; Zhang et al., 2014). These transformation strategies, especially the continuous expression of specific TFs, may confer EMT resistance to RPE cells *in vivo*. This prompted us to screen and identify core TFs that induce MET in dedifferentiated iPSC-RPE (De-iPSC-RPE) cells. In addition, we investigated the mechanisms underlying the TF-mediated transformation and evaluated the anti-EMT function, therapeutic function, and safety of TF-induced iPSC-RPE cells.

RESULTS

Combination of CRX, MITF-A, NR2E1, and C-MYC induces MET in De-iPSC-RPE cells

Human umbilical cord mesenchymal stem cells (hUCMSCs) were reprogrammed into iPSCs (Figures S1A–S1C). Mature iPSC-RPE cells derived from iPSCs demonstrated polygonal morphology (Figure S1D). To simply and quickly acquire De-iPSC-RPE cells, we cultured iPSC-RPE cells in a medium containing fetal bovine serum (FBS), the cells lost their polygonal morphology and exhibited an irregular or elongated mesenchymal shape (Figure S1E), indicating that iPSC-RPE cells underwent EMT.

To investigate whether retinal TFs could induce a direct and rapid MET process in De-iPSC-RPE cells, we carefully selected a set of 11 different retinal TFs (*crx*, *mitf-a*, *nr2e1*, *c-myc*, *lhx2*, *otx2*, *pax6*, *klf4*, *rax*, *sox2*, and *six6*) based on their expression and function during retinal development. The entire process is illustrated in Figure 1A. A cocktail of all TF-expressing retroviruses was used to transfect De-iPSC-RPE cells. After seven days, five clones with cells showing polygonal or mesenchymal morphology were picked with cloning rings for expansion and were evaluated for RPE-specific and EMT-specific markers (Figure S2). Quantitative real-time polymerase chain reaction (qRT-PCR) revealed that RPE-specific markers were markedly upregulated in clone 11TFs-1 with polygonal morphology. In contrast, the expression of genes associated with EMT (*fn1* and *α-sma*) was dramatically downregulated in clone 11TFs-1 compared with that in De-iPSC-RPE cells (Figure S2). Because among the five clones, only clone 11TFs-1 expressed high levels of all RPE specific markers, low levels of both EMT markers, and exhibited RPE-like polygonal morphology (Figure S2), the combination of exogenous TFs in clone 11TFs-1 should be the optimal TF combination to drive MET in De-iPSC-RPE cells.

Thereafter, we evaluated the expression of exogenous TFs in each clone and found that exogenous TFs were heterogeneously expressed among different clones (Figure S2). The expression of *c-myc*, *nr2e1*, *crx*, *mitf-a*, *pax6*, *lhx2*, and *otx2* was higher in clone 11TFs-1 (Figure S2), suggesting that this combination of TFs may be sufficient to drive MET in De-iPSC-RPE cells. Thus, we used a combination of these seven TFs to transfect De-iPSC-RPE cells, and gene expression analyses clearly indicated that this combination was sufficient to induce the MET process (Figure S3A). Furthermore, considering that *pax6* may induce neural retina development, we excluded it from the TF combination and found that the remaining six TFs were able to robustly induce the generation of RPE cell colonies with polygonal morphology (Figure S3B).

Subsequently, we confirmed that *lhx2* and *otx2* were not essential for inducing MET (Figures S3C and S3D). Thus, the combination of four TFs, namely *c-myc*, *crx*, *mitf-a*, and *nr2e1*, may efficiently induce MET in De-iPSC-RPE cells. Hence, we investigated the specific requirements for each TF by performing "N minus 1" experiments. 4TFs clones and "4TFs minus 1" clones were picked out and the gene expression was analyzed by qRT-PCR (Figure S4), and the results demonstrated that 4TFs clones exhibited polygonal morphology and expressed high levels of RPE-specific markers and markedly low levels of EMT markers (Figures S4C and S4D). We further compared the gene expression patterns of "4 TFs minus 1"-RPE cells with 4TFs-RPE cells by RNA-seq analysis. Pearson correlation analysis revealed a strong correlation between repeated samples (Figure S5A); hence, we selected 4TFs-1, 4TFs−mitf-a-1, 4TFs−crx-1, 4TFs−nr2e1-1, and 4TFs−c-myc-1 RPE cells for subsequent experiments. Western blotting demonstrated that only 4TFs-RPE cells expressed all RPE specific markers RPE65, BEST1, TYRP1, MERTK, and did not express EMT marker FN1 (Figures S5B and S5C). One of the functions of RPE cells is to clear the photoreceptor outer segments (POS) that are shed daily by photoreceptors mediated by microvilli (Strauss, 2005). In addition, transepithelial electrical resistance (TER) and cell permeability are used to evaluate epithelial integrity of RPE cells (Rong and Liu, 2011). Results showed that 4TFs-RPE cells phagocyted more POS, exhibited higher TER and lower permeability than "4TFs minus 1" RPE cells (Figures S5D–S5G). These data collectively revealed that any combination of "4TFs minus 1" did not induce a complete functional RPE phenotype in De-iPSC-RPE cells, and CRX, MITF-A, NR2E1, and C-MYC were essential and necessary to induce a complete functional RPE phenotype in De-iPSC-RPE cells, we defined these cells as induced RPE (iRPE) cells.

iRPE have comparable phenotypes and functions to iPSC-RPE cells

To identify the property of iRPE cells, we firstly compared the gene expression patterns of iPSC-RPE, De-iPSC-RPE, and iRPE cells using RNA-seq analysis. Pearson correlation analysis revealed that the transcriptional profile of iRPE cells was more similar to that of De-iPSC-RPE cells than to that of iPSC-RPE cells after cultured for eight days (Figure S6A). However, in terms of RPE-specific genes, polarity-related genes, and EMT-related genes, hierarchical clustering analysis revealed that iRPE cells were more similar to iPSC-RPE cells than to De-iPSC-RPE cells (Figure S6B). In addition, both analyses revealed a strong correlation between repeated samples; thus, we selected iPSC-RPE-1, De-iPSC-RPE-1, and iRPE-1 cells for subsequent experiments.

We next evaluated the protein expression levels in iRPE cells. Immunostaining showed that iPSC-RPE cells expressed higher RPE-specific markers and lower EMT-specific marker FN1 and α-SMA than De-iPSC-RPE cells (Figure 1B). The iRPE cells exhibited an apparently polygonal morphology with continuous tight junction ZO-1, similar to iPSC-RPE cells, whereas a discontinuous arrangement of ZO-1 was observed in De-iPSC-RPE cells. RPE specific markers RPE65, CRALBP, and TYRP1 were highly expressed in iRPE cells, whereas FN1 and α-SMA were barely detected (Figure 1B), and this was confirmed by western blotting (Figure 1C). We further evaluated the functions of iRPE cells. Transmission electron microscopy (TEM) showed that there were a large number of microvilli on the cell membrane of iPSC-RPE and iRPE cells, whereas there were almost no microvilli on the membrane of De-iPSC-RPE cells (Figure 1D), and the phagocytic capacity of iRPE cells was greater than that of De-iPSC-RPE cells, and was similar to that of iPSC-RPE (Figures 1E and 1F). The monolayer of iRPE cells formed in Transwell inserts possessed a higher TER value and lower permeability than the monolayer of De-iPSC-RPE cells, and a comparable TER value and permeability to those of the monolayer of iPSC-RPE cells (Figures 1G and 1H). The secretion patterns of PEDF and VEGF in iRPE cells were similar to that in iPSC-RPE cells, with a higher concentration of PEDF and a lower concentration of VEGF in the apical media than that in the basal media measured by enzyme-linked immunosorbent assay (ELISA) (Figure 1I). These results collectively confirmed that iPRE cells had similar properties and functions as iPSC-RPE cells.

ARPE19 is an RPE cell line popularly used to clarify RPE functions (Wang et al., 2005). We further compared the properties of iPRE cells with ARPE19. Mature RPE cells contain pigments that absorb scattered light and diminish photo-oxidative stress. After being cultured for one month, iRPE cells developed brown and/or black pigments, similar to iPSC-RPE cells (Figure S7A). However, we did not observe pigment formation in ARPE19 (Figure S7A). In addition, compared with ARPE19, iRPE cells expressed higher levels of RPE specific markers and lower levels of EMT markers (Figures S7A–S7C), possessed more microvilli (Figure S7D) and phagocyted more POS (Figures S7E and S7F), and maintained higher epithelial integrity (Figures S7G–S7I). These results indicated that compared with ARPE19, iRPE cells had more similar properties to

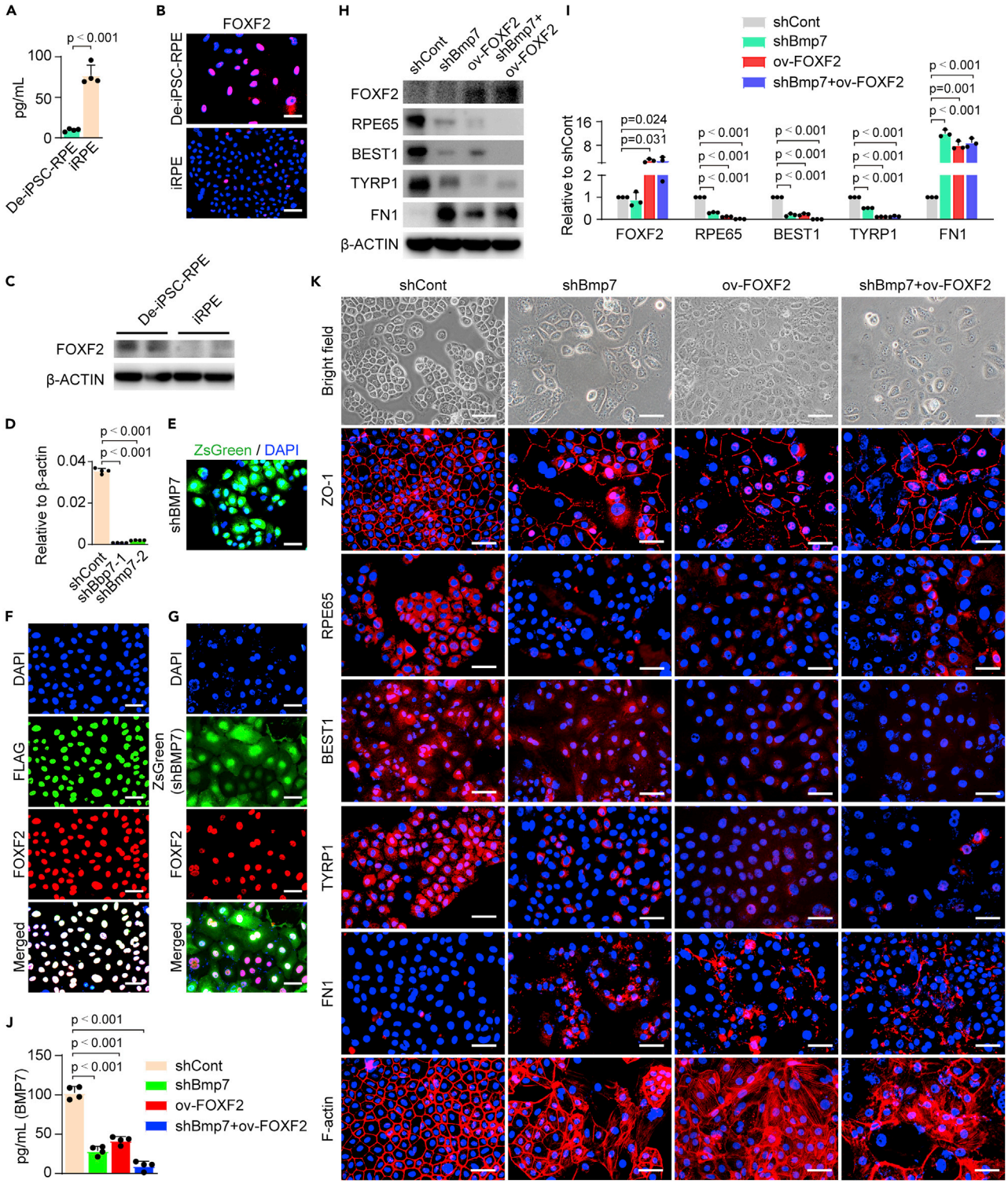

Figure 2. BMP7 and FOXF2 are critical regulators of EMT in iRPE cells

(A) The higher level of BMP7 secreted by iRPE cells compared with De-iPSC-RPE cells was determined by ELISA. Data are mean ± SD, unpaired two-sided t-tests, n = 4.

(B and C) The reduced expression level of FOXF2 in iRPE compared with that in De-iPSC-RPE cells was determined by (B) immunostaining and (C) western blotting. Scale bar = 50 μm.

Figure 2. *Continued*

(D) The efficiency of bmp7 knockdown was determined by qRT-PCR; shBmp7-1 was slightly more efficient at reducing the mRNA level of bmp7 than shBmp7-2; therefore, it was selected for subsequent experiments. Data are mean ± SD, one-way ANOVA and post hoc Bonferroni test, n = 4.

(E) The shBmp7 construct contained the ZsGreen expression element to indicate successful transfection. Scale bar = 50 μm. (F and G) FLAG-FOXF2 overexpression (ov-FOXF2) in (F) iRPE cells (G) shBmp7-iRPE cells. Scale bar = 50 μm.

(H and I) The expression levels of RPE-specific markers and EMT markers were determined by (H) western blotting and (I) quantitative analysis. Data are mean ± SD, one-way ANOVA and post hoc Bonferroni test, n = 3.

(J) BMP7 expression levels in shCont-iRPE, shBmp7-iRPE, ov-FOXF2- iRPE, and shBmp7 + ov-FOXF2-iRPE. Data are mean ± SD, one-way ANOVA and post hoc Bonferroni test, n = 4.

(K) The immunostaining of RPE-specific markers and EMT markers. Overexpression of FOXF2 exhibited similar effects to knockdown of *bmp7* in iRPE cells by downregulating RPE markers and upregulating EMT marker. Scale bar = 50 μm.

iPSC-RPE cells. We further introduced 4TFs into ARPE19, and obtained ARPE19-derived iRPE cells, named AD-iRPE cells (Figure S8A). The cells showed polygonal morphology, higher expression of CRALBP, TYRP1, and lower expression of FN1 compared with ARPE19 (Figures S8B–S8D). In addition, AD-iRPE cells phagocyted more POS (Figures S8E and S8F) and had higher TER than ARPE19 (Figure S8G). These results suggested that 4TFs improved the epithelial phenotype of ARPE19.

BMP7, forkhead box F2(FOXF2), LIN7A, and PARD6B are critical regulators for maintaining epithelial phenotype and integrity of iRPE cells

iRPE cells maintained the epithelial phenotype even in FBS-containing medium, which prompted us to clarify the mechanism by which iRPE cells maintain the epithelial phenotype. We used RNA-seq data to identify differentially expressed genes (DEGs) in iRPE cells compared with De-iPSC-RPE cells. Based on the threshold criteria, a total of 3,304 DEGs were identified, of which 1,645 genes were upregulated and 1,659 genes were downregulated in iRPE cells compared with De-iPSC-RPE cells (Figure S9A). Gene ontology (GO) enrichment analysis of these genes using the GO database revealed 34 EMT-related genes (Figures S9B and S9C). We selected eight genes for verification by qRT-PCR (Figure S9D). Among the 34 genes, the difference in *bmp7* and *foxf2* levels was the highest between iRPE and De-iPSC-RPE cells (Figure S9C). In addition, previous work reported that BMP7 was an EMT repressor (Yao et al., 2019) and FOXF2 is an EMT inducer (Meyer-Schaller et al., 2018); hence, we focused on these two genes to clarify their functions in maintaining epithelial phenotype of iRPE cells.

We observed that the protein level of BMP7 was higher, and FOXF2 was lower in iRPE cells compared with that in De-iPSC-RPE cells (Figures 2A–2C). Thereafter, we firstly downregulated *bmp7* in iRPE cells by transfecting them with lentiviral particles expressing two different shRNAs against *bmp7*. Among the two shRNAs, shBmp7-1 was marginally more efficient at reducing the mRNA level of *bmp7* than shBmp7-2 (Figure 2D); hence, we selected shBmp7-1-transfected iRPE (shBmp7-iRPE) cells for subsequent experiments. ZsGreen+ cells, indicating successful transfection, were sorted by flow cytometry and cultured in a dish (Figure 2E). We next overexpressed FLAG-FOXF2 in iRPE cells or shBmp7-iRPE cells (Figures 2F and 2G) and verified FOXF2 levels in these cells by western blotting (Figures 2H and 2I). In addition to marked reduction in BMP7 levels by shBmp7 (Figure 2J), FOXF2 overexpression downregulated the expression of BMP7 in iRPE cells (Figure 2J). BMP7 deficiency resulted in reduced expression of RPE-specific markers and increased expression of the EMT marker FN1 (Figures 2H and 2I). Overexpression of FOXF2 in iRPE cells exhibited similar effects as *bmp7* knocked down in iRPE cells and further downregulated RPE markers in shBmp7-iRPE cells (Figures 2H and 2I), suggesting a synergistic effect of *bmp7* knockdown and FOXF2 overexpression in the induction of EMT in iRPE cells. Immunostaining revealed similar results, and F-actin transformed from the circumferential actin belt into stress fibers in iRPE cells with *bmp7* knockdown and/or overexpression of FOXF2 (Figure 2K). These results suggest that BMP7 and FOXF2 are critical negative and positive regulators of EMT, respectively, and upregulated expression of BMP7 and downregulated expression of FOXF2 are essential for iRPE cell maintaining epithelial phenotype.

RPE cells constitute a highly polarized monolayer with barrier function by cell junctions, such as tight junctions. The premise of RPE cells playing barrier function is to maintain epithelial phenotype and integrity, and a group of polarity protein complexes, such as the Crumbs, PAR, and Scribble complexes, are not only necessary to maintain polarity, but can also regulate cell junction assembly and maintain the integrity of epithelial cells (Bazzoun et al., 2013; Martin et al., 2021). To investigate which polarity proteins participate in iRPE cell junction maintenance and epithelial integrity, we performed GO enrichment analysis of the polarity-related genes among the DEGs (iRPE cells vs. De-iPSC-RPE cells) and identified 30 genes

(Figures S9A and S9E and S9F). Among these, *lin7a*, *pard6b*, and *dlg1* belong to the Crumbs, PAR, and Scribble complexes, respectively. *Lin7a* and *Pard6b* were upregulated, whereas *Dlg1* was downregulated in iRPE cells compared with De-iPSC-RPE cells (Figure 3F), indicating that *lin7a* and *pard6b* may play critical roles in maintenance of cell junctions and epithelial integrity of iRPE cells. Therefore, we focused on *lin7a* and *pard6b*, and their expression levels in iRPE and De-iPSC-RPE cells were further verified by qRT-PCR (Figure S9G), immunostaining (Figure 3A), and western blotting analysis (Figure 3B). Thereafter, we downregulated *lin7a* and *pard6b* in the iRPE cells (Figures 3C and 3D) and selected iRPE cells with shLin7a-2 or shPard6b-1 deficiency for the subsequent experiments, and termed them shLin7a-iRPE cells and shPard6b-iRPE cells, respectively. shLin7a and shPard6b markedly reduced the protein levels of LIN7A and PARD6B (Figures 3E–3J). We performed myosin staining to clarify the morphological changes in the iRPE cells. Myosin is localized in the apical and lateral membrane and associated with adherens junctions (Curran et al., 2017; Zihni et al., 2017). Immunostaining revealed that shCont-iRPE cells maintained a regular polygonal morphology whereas iRPE cells with LIN7A or PARD6B deficiency exhibited non-polygonal morphology with space between cells at three-fold vertices (Figure 3K). We further analyzed ZO-1 expression and found that it formed a continuous tight junction between shCont-iRPE cells; in contrast, higher number of discontinuous junctions at three-fold vertices were observed in iRPE cells with LIN7A or PARD6B deficiency than that in shCont-iRPE cells (Figures 3K and 3L). These results suggest that LIN7A and PARD6B are positive regulators of tight junctions. In addition, the monolayer of shCont-iRPE cells possessed a higher TER value and lower permeability than the monolayer of iRPE cells with LIN7A or PARD6B deficiency (Figures 3M and 3N). These results indicate that LIN7A and PARD6B positively regulate the integrity of iRPE cells. Overall, BMP7, FOXF2, LIN7A, and PARD6B are critical regulators for maintaining epithelial phenotype and integrity of iRPE cells.

PPM1A confers TGF-β-induced EMT resistance in iRPE cells

iPSC-RPE cells easily undergo EMT when cultured in an FBS-containing medium, demonstrating that FBS contains an EMT inducer. However, the iRPE cells were able to maintain the epithelial phenotype in the FBS-containing medium, indicating that they were resistant to EMT. TGF-β is upregulated in the retina in AMD and plays a dominant role in inducing EMT in RPE cells, which is thought to be an essential etiology of AMD (Wang et al., 2019). To investigate whether iRPE cells were resistant to EMT induced by TGF-β1 or TGF-β2, we treated iRPE cells with TGF-β1 or TGF-β2 *in vitro* to simulate the hostile microenvironment *in vivo* for eight days, using iPSC-RPE cells as a control. We found that iPSC-RPE cells lost their polygonal morphology and became mesenchymal morphology when treated with TGF-β1 or TFG-β2, indicating the occurrence of EMT (Figure 4A). However, iRPE cells maintained their polygonal morphology with or without TGF-β1 or TGF-β2 treatment (Figure 4A), it was further confirmed by ZO-1 staining that discontinuous ZO-1 staining was observed in iPSC-RPE cells treated with TGF-β1 or TGF-β2, but not in iRPE cells (Figure 4A). In addition, RPE-specific proteins were dramatically downregulated and EMT-related markers were markedly upregulated in iPSC-RPE cells after TGF-β1 or TGF-β2 treatment, whereas nearly no change was noted in the levels of these proteins in iRPE cells (Figure 4A). Consistent with the immunostaining results, qRT-PCR analysis further confirmed that iRPE cells were resistant to TGF-β1 or TGF-β2 induction (Figure 4B).

Phosphorylation of SMAD2/3 is a classical characteristic of TGF-β-induced EMT (Wang et al., 2019). We found that TGF-β1 or TGF-β2 markedly triggered the phosphorylation of SMAD2 in iPSC-RPE cells but not in iRPE cells (Figure 5A). These results indicate that the anti-EMT function may be mediated, at least in part, by blocking the phosphorylation of SMAD2 in iRPE cells. PPM1A, a phosphatase, can reportedly dephosphorylate pSMAD2 (Lin et al., 2006), and we found that PPM1A was highly expressed in iRPE cells compared with iPSC-RPE cells at day 1 after subcultured (Figures 5B and 5C). This indicates that PPM1A may mediate the dephosphorylation of pSMAD2 in iRPE cells. Thereafter, we downregulated the expression of PPM1A in iRPE cells. The qRT-PCR results revealed that shPpm1a-2 was more efficient at reducing the mRNA level of *ppm1a* than shPpm1a-1 (Figure 5D); therefore, we selected iRPE cells with shPpm1a-2 deficiency for the subsequent experiments and termed shPpm1a-iRPE cells. Compared with scramble shRNA (shCont), shPpm1a markedly reduced the protein level of PPM1A in iRPE cells (Figures 5E–5G). Furthermore, we treated shCont-iRPE and shPpm1a-iRPE cells with TGF-β1 or TGF-β2. An increased level of pSMAD2 was observed in shPpm1a-iRPE cells but not in shCont-iRPE cells (Figure 5H), which was confirmed by western blotting (Figures 5I–5L). This indicates that TGF-β was able to activate the phosphorylation of SMAD2 in shPpm1a-iRPE cells but not in shCont-iRPE cells, and PPM1A mediates the dephosphorylation of SMAD2 in iRPE cells. Immunostaining revealed that *ppm1a* knockdown along with TGF-β1 or TGF-β2 treatment resulted in decreased expression of RPE markers, increased expression of the

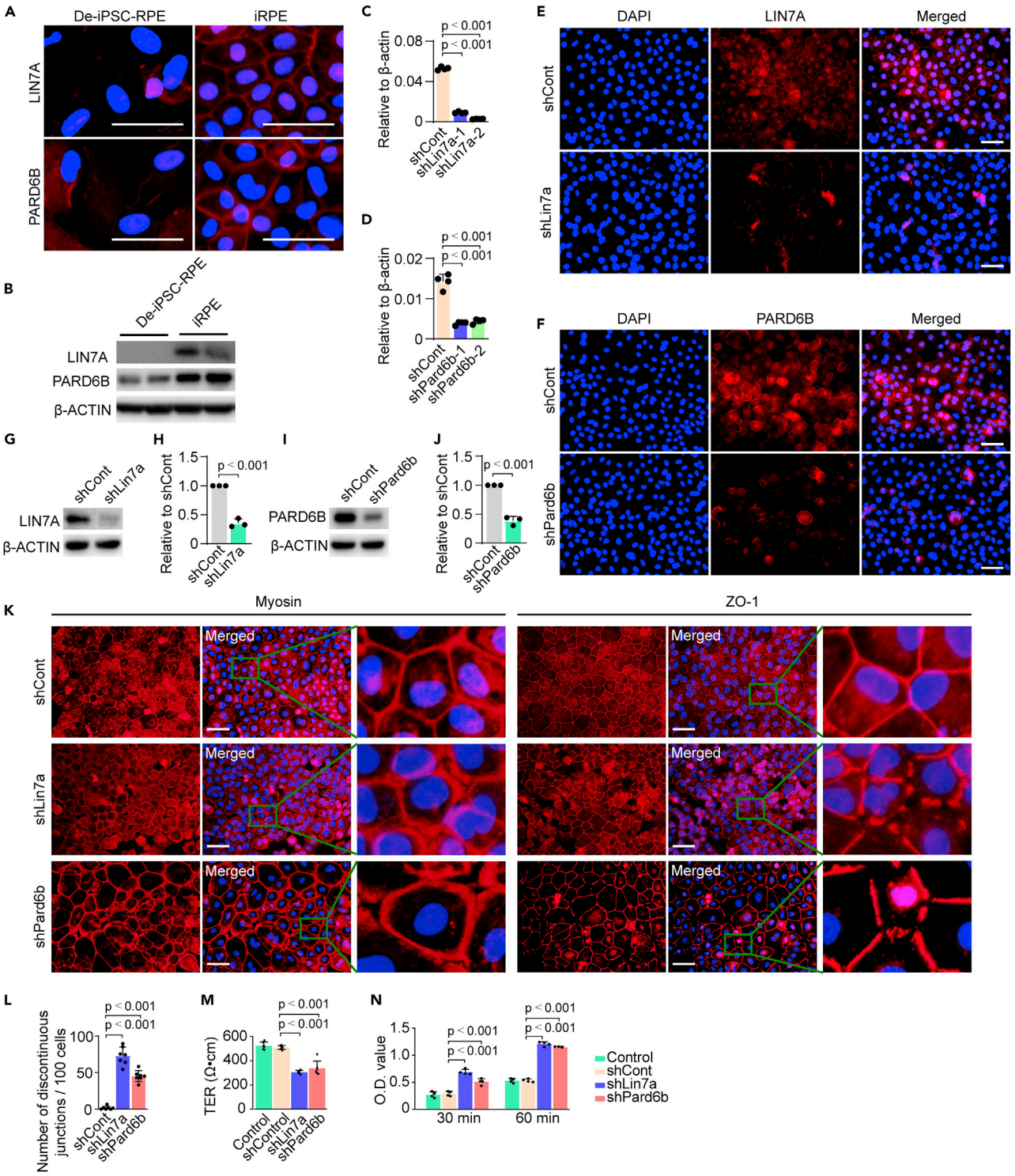

Figure 3. LIN7A and PARD6B are critical for iRPE cell integrity maintenance

(A and B) The decreased expression levels of LIN7A and PARD6B in iRPE compared with that in De-iPSC-RPE cells were demonstrated by (A) immunostaining and (B) western blotting. Scale bar = 50 μm.

(C and D) Knockdown efficiency of (C) lin7a and (D) pard6b was determined by qRT-PCR; as shLin7a-2 and shPard6b-1 were most efficient at reducing the mRNA levels of lin7a and pard6b, these were selected for subsequent experiments. Data are mean ± SD, one-way ANOVA and post hoc Bonferroni test, n = 4.

Figure 3. *Continued*

(E–J) The expression levels of LIN7A and PARD6B after knockdown in iRPE cells were verified by (E and F) immunostaining and confirmed by (G-J) western blotting and quantitative analysis. Scale bar = 50 μm. Data are mean ± SD, unpaired two-sided t-tests, n = 3.

(K and L) Cell morphology and tight junction were demonstrated by myosin and ZO-1 immunostaining (K), and the Quantitative analysis of discontinuous tight junctions at three-fold vertices was determined as number of discontinuous junctions per 100 cells (L). Scale bar = 50 μm. Data are mean ± SD, one-way ANOVA and post hoc Bonferroni test, n = 8.

(M and N) The damaged epithelial integrity in iRPE cells with LIN7A or PARD6B deficiency was evaluated by TER analysis (M), n = 6, and HRP permeability assay (N), n = 4. Data are mean ± SD, one-way ANOVA and post hoc Bonferroni test.

EMT marker α-SMA, and stress fiber formation in shPpm1a-iRPE cells (Figure 5H). The expression levels of RPE markers and the EMT marker, α-SMA, and stress fiber formation did not differ between shCont-iRPE cells treated with or without TGF-β1 or TGF-β2 (Figure 5H). We further overexpressed FLAG-PPM1A in iRPE cells and verified binding between PPM1A and SMAD2 by co-immunoprecipitation (Co-IP, Figure 5M). Furthermore, we observed that the phosphorylation of SMAD3 was repressed in iRPE cells but not in iPSC-RPC cells and shPpm1a-iRPE cells treated with TGF-β1 or TGF-β2 (Figure S10). Collectively, these data indicate that iRPE cells resistance to EMT induction by TGF-β1 or TGF-β2 is achieved, or at least partially, by PPM1A-mediated dephosphorylation of molecules, such as SMAD2 and/or SMAD3, in TGF-β signaling pathway.

MITF-A, CRX, NR2E1, and C-MYC transcriptionally regulate *bmp7*, *foxf2*, *lin7a*, *pard6b*, and *ppm1a* in a direct or indirect pattern

Overexpression of MITF-A, CRX, NR2E1, and C-MYC allowed iRPE cells to acquire and maintain epithelial property, the four TFs must regulate *bmp7*, *foxf2*, *lin7a*, *pard6b*, and *ppm1a* directly or indirectly. To investigate the regulatory relationship between these four TFs and the five essential genes, we compared the protein levels of BMP7, FOXF2, LIN7A, PARD6B, and PPM1A in "4 TFs minus 1" RPE cells with that in iRPE cells. ELISA results showed that the expression level of BMP7 in "4TFs minus 1" RPE cells was markedly reduced compared with that in iRPE cells (Figure 6A), indicating that all four TFs promoted the expression of BMP7. Western blotting analysis (Figures 6B and 6C) revealed that the protein level of FOXF2 was increased significantly in 4TFs−crx-RPE and 4TFs−c-myc-RPE cells, indicating that CRX and C-MYC repressed the expression of FOXF2. The expression level of LIN7A was higher in 4TFs−mitf-a-RPE and 4TFs−nr2e1-RPE cells and lower in 4TFs−crx-RPE cells than that in iRPE cells, suggesting that LIN7A expression was repressed by MITF-A and NR2E1 but promoted by CRX, further demonstrating that the TFs have opposite regulatory functions. Furthermore, the expression of PARD6B in 4TFs−crx-RPE and 4TFs−c-myc-RPE cells was reduced compared to that in iRPE cells, indicating that CRX and C-MYC promoted PARD6B expression. In addition, we observed that the expression level of PPM1A was lower in 4TFs−crx-RPE cells than that in iRPE cells, suggesting that CRX promotes PPM1A expression.

To clarify whether the four TFs transcriptionally regulate the five critical genes directly, we generated FLAG-MITF-A-iRPE, FLAG-CRX-iRPE, FLAG-NR2E1-iRPE, and FLAG-C-MYC-iRPE cells by co-transfection of the four TFs with one of them being FLAG-tagged TF in each cell line, and performed chromatin immunoprecipitation assay with sequencing (ChIP-seq) analysis. All combinations of FLAG-TF and the other three TFs successfully converted the De-iPSC-RPE cells into iRPE cells with polygonal morphology (Figure 6D). ChIP-seq analysis revealed that CRX targets *bmp7*, *lin7a*, *pard6b*, and *ppm1a* directly (Figures 6E–6H), and this was further confirmed by ChIP-PCR analysis (Figure 6I). MITF-A and NR2E1 transcriptionally regulated *lin7a* directly (Figures 6J–6M). In addition, ChIP-seq analysis revealed indirect transcriptional regulation of *foxf2*, *bmp7*, and *pard6b* in iRPE cells. CRX did not bind to the promoter region of *foxf2* (Figure S11A); MITF-A and NR2E1 did not bind to the promoter regions of *bmp7* (Figure S11A). Although MITF-A and NR2E1 bound to the *pard6b* promoter (Figures S11A and S11B), they did not change the expression level of PARD6B in iRPE cells (Figures 6B and 6C). We observed that C-MYC did not bind to the promoter regions of *foxf2*, *bmp7*, *lin7a*, *pard6b*, and *ppm1a* (Figures S11A and S11C), and C-MYC bound to the promoter regions of *ccnd1*, confirming its role in promoting cell proliferation (Figures S11C and S11D). The regulatory relationships between the four TFs and the five critical genes have been delineated in a schematic model (Figure 6N).

Combination of the four TFs, among which *c-myc* regulated by a Tet-on system, converts De-iPSC-RPE cells into iRPE cells

Exogenous C-MYC expression is essential for reprogramming somatic cells into iPSCs, and its absence in the reprogramming cocktail reduces reprogramming efficiency (Nakagawa et al., 2008). Our results

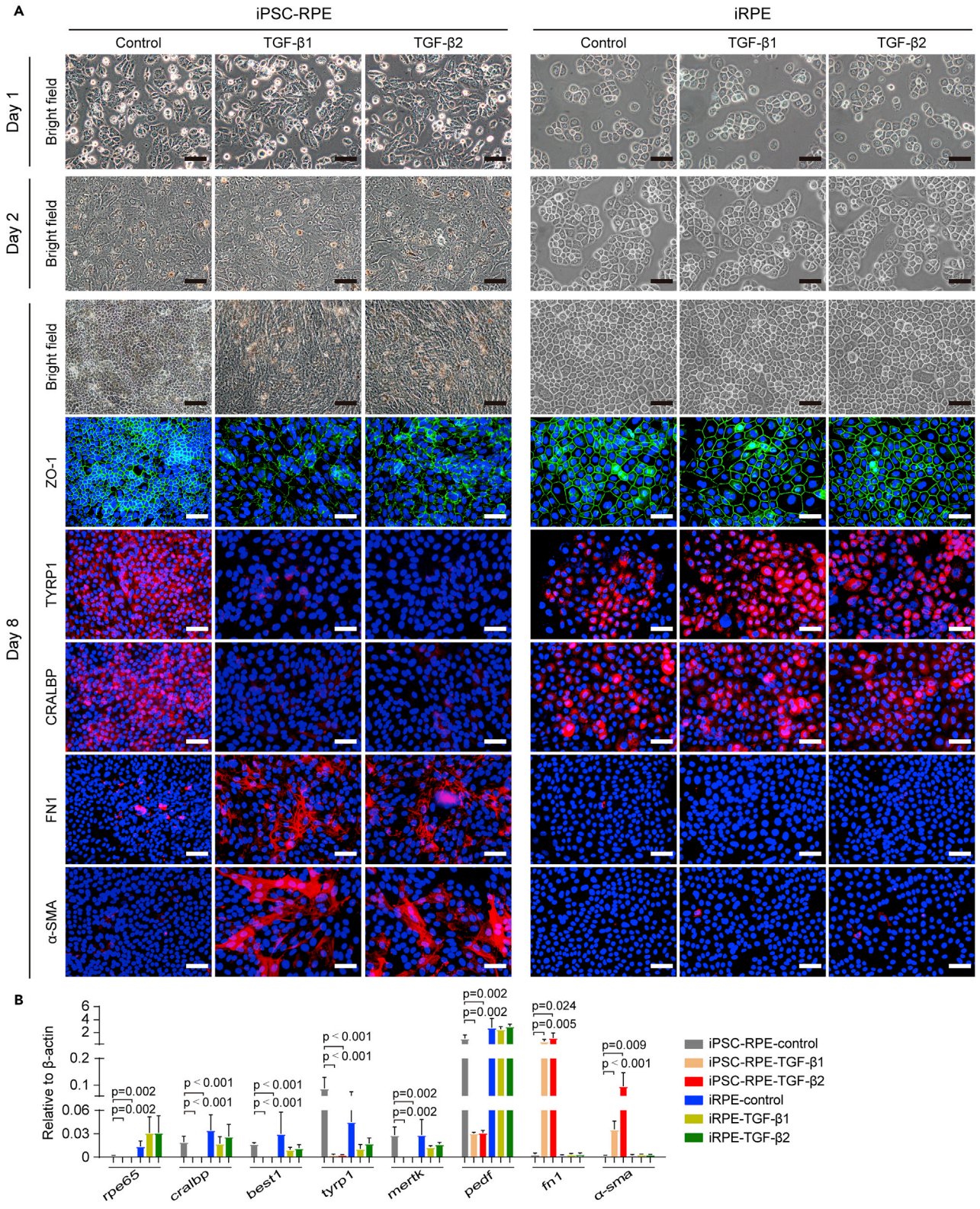
A
iPSC-RPE
iRPE
Control
TGF-β1
TGF-β2
Day 1
Day 2
Day 8
Bright field
ZO-1
TYRP1
CRALBP
FN1
α-SMA
B
Relative to β-actin
rpe65
cralbp
best1
tyrp1
mertk
pedf
fn1
α-sma
iPSC-RPE-control
iPSC-RPE-TGF-β1
iPSC-RPE-TGF-β2
iRPE-control
iRPE-TGF-β1
iRPE-TGF-β2

Figure 4. iRPE cells possess anti-EMT property

(A) iPSC-RPE cells and iRPE cells were subjected to TGF-β1 or TGF-β2 induction for 8 days. Bright-field images and immunostaining showed that TGF-β induction led to EMT in iPSC-RPE cells, as indicated by loss of polygonal morphology and reduced expression of RPE markers and increased expression of EMT markers; however, iRPE cells showed no such changes, indicating anti-EMT property. Scale bar = 50 μm.

(B) The qRT-PCR analysis demonstrated that the expression levels of RPE markers and EMT markers were altered in iPSC-RPE cells but not in iRPE cells after treated with TGF-β1 or TGF-β2. Data are mean ± SD, one-way ANOVA and post hoc Bonferroni test, n = 3.

demonstrated that C-MYC did not directly regulate the aforementioned five critical genes; therefore, we hypothesized that C-MYC may promote the efficiency of transforming De-iPSC-RPE cells into iRPE cells, instead of regulating the EMT pathway in iRPE cells. We used a Tet-on regulatory system to regulate *c-myc* expression. The combination of Tet-on-C-MYC, MITF-A, CRX, and NR2E1 successfully transformed De-iPSC-RPE cells into iRPE cells with canonical polygonal morphology (Figure 7A). Because doxycycline (Dox) was used to trigger *c-myc* expression in these iRPE cells, we termed them Dox-iRPE cells. We found that Dox promoted the proliferation of Dox-iRPE cells in a dose-dependent manner up to 0.5 mg/mL, but Dox was cytotoxic at a concentration of 2 mg/mL (Figure 7B). The expression level of *c-myc* was proportional to Dox concentration (Figure 7C). Even after removal of Dox from the culture medium, Dox-iRPE cells expressed higher levels of RPE-specific markers and lower levels of EMT markers compared to that in De-iPSC-RPE cells (Figures 7D and 7E). In addition, Dox-iRPE cells were able to maintain the epithelial phenotype and inhibit the TGF-β1- or TGF-β2-mediated phosphorylation of SMAD2 in absence of Dox treatment (Figure 7F), suggesting that Dox-iRPE cells were resistant to TGF-β-induced EMT.

C-myc is an oncogene, and continuous expression of C-MYC favors oncogenesis (Nesbit et al., 1999). Thus, Dox-iRPE cells with lower expression of *c-myc* may be much safer than iRPE cells for *in vivo* transplantation. To determine the safety of iRPE and Dox-iRPE cells, tumorigenicity was examined by subcutaneously transplanting green fluorescent protein (GFP)-tagged iRPE or Dox-iRPE cells embedded in Matrigel into nude mice. GFP-tagged HELA cells were used as positive controls. The results revealed that the grafted cells quickly proliferated under the skin in all HELA-transplanted nude mice, indicated by the formation of a bulge two weeks after transplantation (Figure S12A). However, a large mass was observed under the skin only in one of the iRPE cell-grafted nude mice, whereas no such proliferation was observed in the Dox-iRPE cell-grafted group 4 months after transplantation (Figure S12A). Tumors formed by HELA and iRPE cells could be easily dissected, given their larger size. However, Matrigels with Dox-iRPE cells required careful dissection because of their small size due to the low proliferation capacity *in vivo* (Figure S12A). The tumorigenesis rates of HELA, iRPE, and Dox-iRPE cells are shown in Figure S9B. Tumorigenicity assays were performed for one year, and no tumors were observed in the Dox-iRPE group. All subcutaneous transplants (HELA, iRPE, and Dox-iRPE cells embedded in Matrigel) were subjected to histological examination at the end of the observation period. A large proportion of Ki67-positive cells was observed in HELA and iRPE cell transplants, whereas few cells were Ki67-positive in Dox-iRPE cell transplants (Figures S12C and S12D). Interestingly, grafted Dox-iRPE cells formed tube-like structures with tight junctions between adjacent cells, as revealed by ZO-1 immunostaining (Figure S12E). In addition, Dox-iRPE cells expressed RPE65 instead of EMT markers FN1 and α-SMA (Figure S12E). Overall, these results suggest that exogenous C-MYC is not an essential factor for maintaining the epithelial phenotype of iRPE cells and that Dox-iRPE cells are much safer than iRPE cells for *in vivo* transplantation.

Dox-iRPE cells protect visual function and retinal structure in rat AMD model

The ultimate goal for the generation of iRPE cells is the development of a more effective and consistent therapy for AMD. Dox-iRPE cells also had anti-EMT function and were safer than iRPE cells (Figure 7 and Figure S12), Therefore, the therapeutic effects of Dox-iRPE cells were evaluated in rat AMD model induced by sodium iodate. The Dox-iRPE cells were grafted into subretinal space of rats. The b-wave amplitude is used to indicate the electroretinogram (ERG) response (Wang et al., 2017). We observed that the b-wave amplitudes of ERG in the iPSC-RPE and Dox-iRPE transplantation groups were much higher than those in the control (phosphate-buffered saline, PBS) group (Figures 8A and 8B). In addition, Dox-iRPE cells protected visual function more efficiently than iPSC-RPE cells (Figures 8A and 8B). Reduction or loss of the outer nuclear layer (ONL) or photoreceptors is a major pathological change in the rat AMD model (Guan et al., 2013). The ONL thickness in the Dox-iRPE group was significantly greater than that in the PBS-treated control and iPSC-RPE-grafted groups at week 6 after transplantation (Figures 8C and 8D), indicating the stronger protective function of Dox-iRPE cells. Terminal deoxynucleotidyl transferase-mediated deoxyuridine triphosphate nick and labeling (TUNEL) analysis performed at week 6 after transplantation showed that the number of apoptotic photoreceptor cells in the ONL in the cell transplantation group

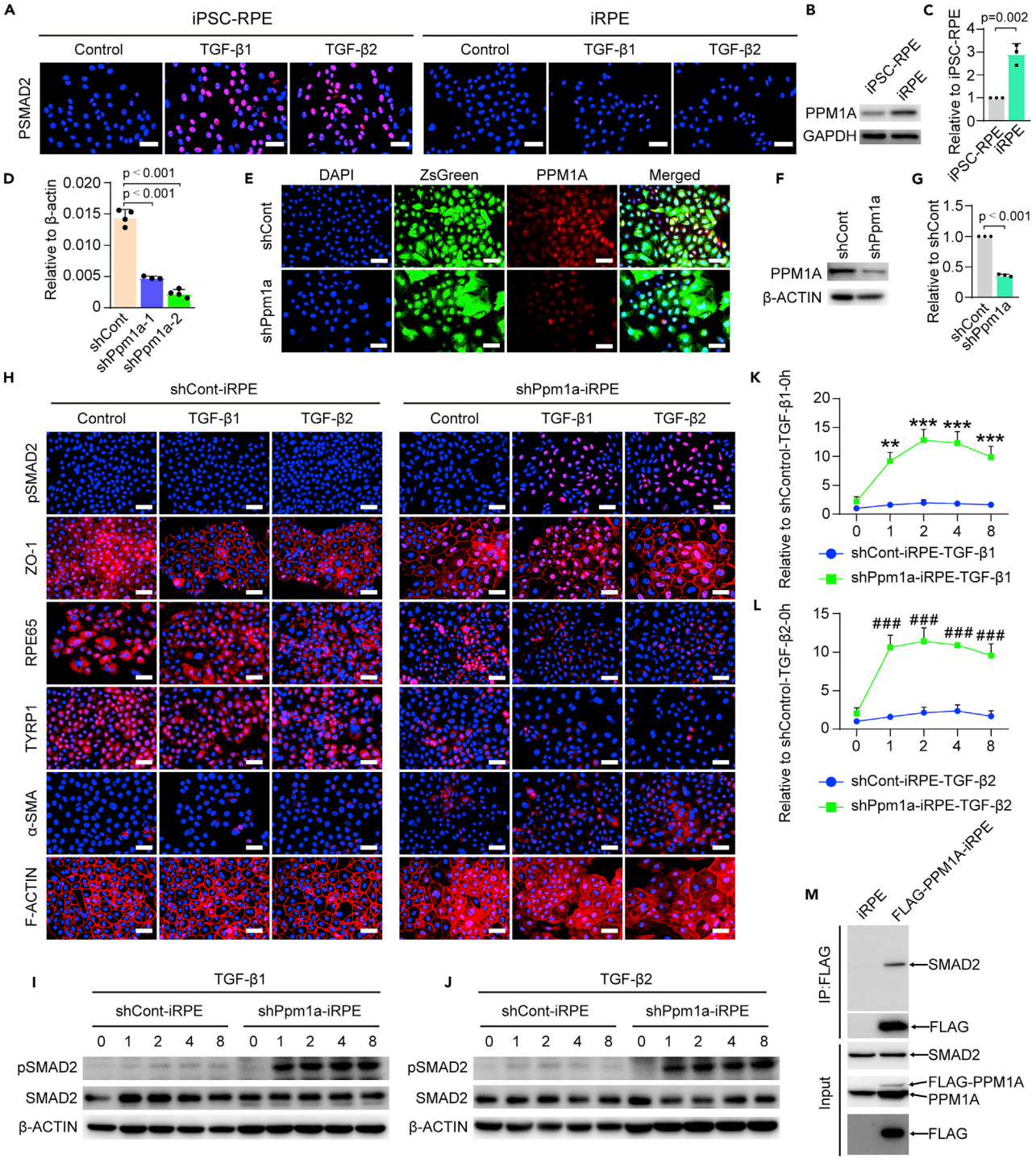

Figure 5. PPM1A confers anti-EMT property in iRPE cells

(A) pSMAD2 was observed in iPSC-RPE but not in iRPE cells treated with TGF-β1 or TGF-β2 after cells were subcultured for one day and determined by immunostaining. Scale bar = 50 μm.

(B and C) The decreased expression level of PPM1A in iPSC-RPE compared with that in iRPE cells was determined by (B) western blotting and (C) quantitative analysis. Data are mean ± SD, unpaired two-sided t-tests, n = 3.

(D) Ppm1a knockdown efficiency was determined by qRT-PCR; shppm1a-2 was most efficient at reducing the mRNA level of ppm1a; hence, we selected shppm1a-2 for the subsequent experiments. Data are mean ± SD, one-way ANOVA and post hoc Bonferroni test, n = 4.

Figure 5. *Continued*

(E–G) The expression level of PPM1A after knockdown in iRPE cells was determined by (E) immunostaining, (F) western blotting, and (G) quantitative analysis. Scale bar = 50 μm. Data are mean ± SD, unpaired two-sided t-tests, n = 3.

(H) The phosphorylation of SMAD2, downregulated RPE markers, and upregulated EMT markers were observed by immunostaining in shPard6b-iRPE cells after treated with TGF-β1 or TGF-β2. Scale bar = 50 μm.

(I–L) Western blotting and quantitative analysis demonstrated that TGF-β1 or TGF-β2 markedly activated the phosphorylation of SMAD2 in shPpm1a-iRPE cells but not in shCont-iPRE cells. Data are mean ± SD, one-way ANOVA and post hoc Bonferroni test, n = 3. **p < 0.01, ***p < 0.001 compared with shPpm1a-iRPE-TGF-β1-0h, ###p < 0.001 compared with shPpm1a-iRPE-TGF-β2-0h.

(M) Western blotting analysis using the indicated antibodies on FLAG immunoprecipitates from iRPE and FLAG-PPM1A-iRPE cells indicated that PPM1A binds SMAD2.

was significantly lower than that in the PBS group, especially in the Dox-iRPE cell transplantation group (Figures 8E and 8F). We next assessed whether the grafted cells underwent EMT in the subretinal space. The results revealed that most grafted iPSC-RPE cells highly expressed EMT marker α-SMA (Figure 8G). However, Dox-iRPE cells continuously expressed RPE specific markers instead of α-SMA (Figure 8G). In addition, Dox-iRPE cells showing Rhodopsin + staining indicated the phagocytic function of the cells (Figure 8G). These results suggest that the more efficient therapeutic functions of Dox-iRPE cells compared with iPSC-RPE cells may be because of their anti-EMT capacity.

Furthermore, when iPSC-RPE cells were grafted into the vitreous cavity for two weeks, the cells expressed EMT marker α-SMA and formed an ERM-like structure, indicating that iPSC-RPE cells underwent EMT (Figure 8H). However, intravitreally grafted Dox-iRPE cells aggregated and were found to be negative for α-SMA, and did not form an ERM-like structure (Figure 8H). This further indicates that the Dox-iRPE cells are safe for subretinal space transplantation by avoiding the formation of ERM because of the probable leakage of RPE cells from subretinal space into vitreous cavity.

DISCUSSION

We successfully converted De-iPSC-RPE cells into iRPE cells using a cocktail of four critical TFs. iRPE cells exhibited EMT resistance and better therapeutic functions than iPSC-RPE cells in an animal model of retinal degeneration.

Our study revealed that BMP7, FOXF2, LIN7A, PARD6B, and PPM1A are critical for the maintenance of the epithelial phenotype and EMT resistance in iRPE cells. BMP7 belongs to the TGF-β superfamily. A previous study demonstrated that BMP7 could maintain the RPE cell phenotype and counteract TGF-β2-induced EMT (Yao et al., 2019). Knockdown of bmp7 resulted in EMT of iRPE cells, suggesting that BMP7 may suppress EMT in iRPE cells through autocrine or paracrine functions. The transcription factor FOXF2 is upregulated during EMT and promotes the expression of Zeb1 and Zeb2, E-cadherin suppressors, to induce EMT (Meyer-Schaller et al., 2018). Overexpression of FOXF2 led to EMT in iRPE cells, confirming the critical role of FOXF2 in EMT in RPE cells. Hence, FOXF2 may be a potential target for inhibiting EMT in RPE cells.

It has been reported that LIN7 has three homologs: LIN7A, LIN7B, and LIN7C. LIN7A is expressed in the retina (Wei et al., 2006). Lin7-knockout mice exhibit abnormalities in epithelial polarization and renal fibrosis (Olsen et al., 2007). However, a previous study showed that hyperproliferation and strong polarity defects in breast carcinogenesis coincided with the high expression of LIN7A (Gruel et al., 2016). Therefore, LIN7A may have a contrasting function in maintaining cell polarity in different tissues, or a specific expression level is required to maintain polarity. Indeed, in iRPE cells, CRX promoted the expression of LIN7A, whereas MITF-A and NR2E1 suppressed the expression of LIN7A, suggesting that CRX, MITF-A, and NR2E1 synergistically maintain the expression level of LIN7A to maintain cell polarity. PAR6 has three homologs: PARD6A, PARD6B, and PARD6G. PARD6B is essential for trophectoderm formation (Alarcon, 2010), and PARD6B deficiency promotes EMT and lung adenocarcinoma cell invasion (Zhou et al., 2017). CRX positively regulates the polarity of iRPE cells by directly promoting the expression of both lin7a and pard6b. Moreover, knockdown of either PAR or Crumbs leads to defects in the polarity of iRPE cells, further confirming that both these polarity protein modules orchestrate epithelial polarity development (Martin et al., 2021).

The classical signaling pathway for TGF-β-induced EMT involves the recruitment and phosphorylation of SMAD2/3 by the TGF-β receptor; the phosphorylated SMAD2/3 recruits SMAD4 to form the SMAD complex that translocates into the nucleus to trigger the expression of EMT-related genes (Zhou et al.,

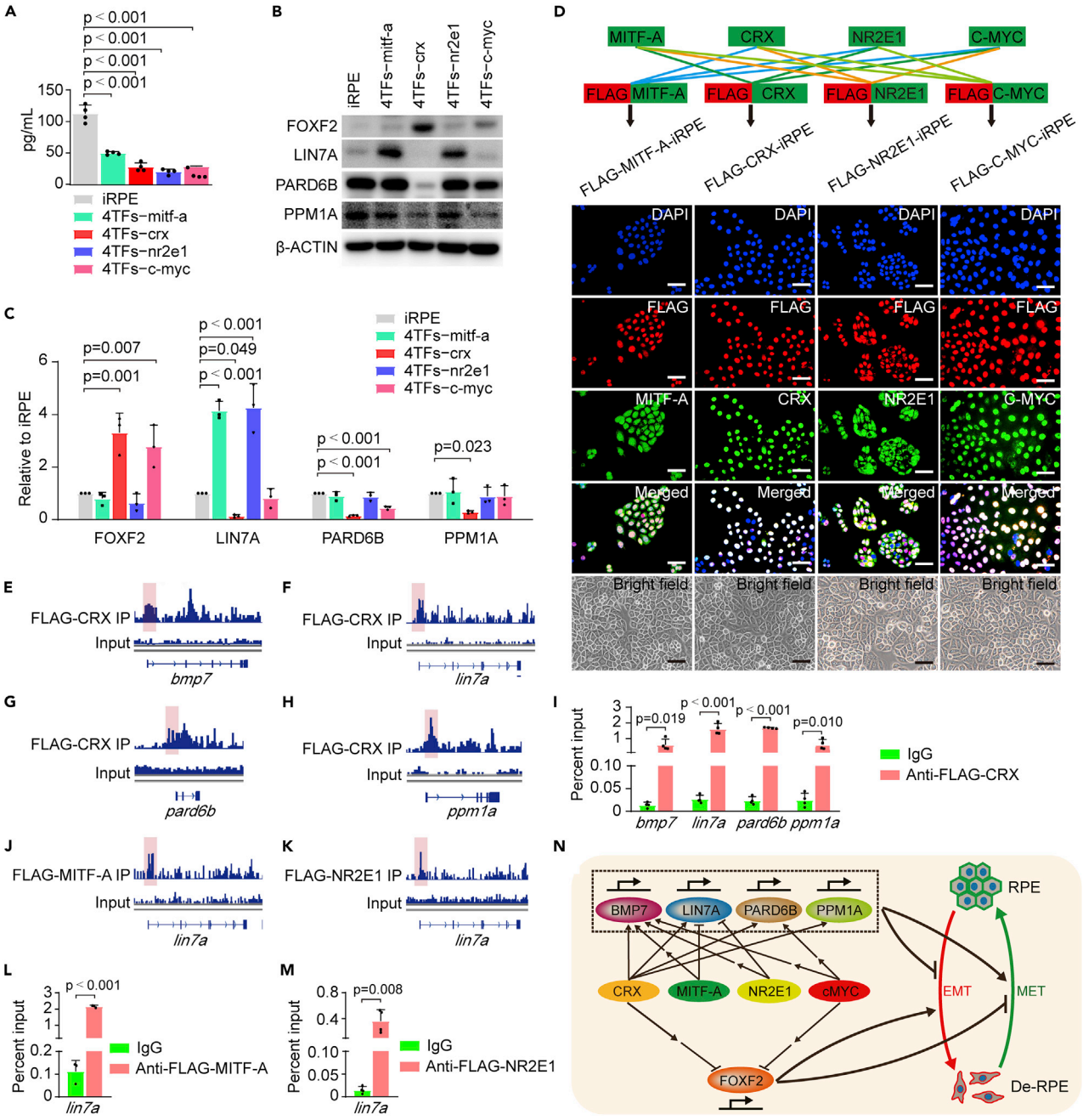

Figure 6. Four TFs transcriptionally regulate *bmp7, foxf2, lin7a, pard6b,* and *ppm1a* in a direct or indirect manner

(A) ELISA analysis demonstrated that BMP7 levels was reduced in 4TFs−nr2e1-RPE, 4TFs−mitf-a-RPE, 4TFs−c-myc-RPE, and 4TFs−crx-RPE cells compared with that in iRPE cells. Data are mean ± SD, one-way ANOVA and post hoc Bonferroni test, n = 4.

(B and C) The levels of FOXF2, LIN7A, PARD6B, and PPM1A were determined by (B) western blotting and (C) quantitative analysis. Data are mean ± SD, one-way ANOVA and post hoc Bonferroni test, n = 3.

(D) Generation of FLAG-MITF-A-iRPE, FLAG-CRX-iRPE, FLAG-NR2E1-iRPE, and FLAG-C-MYC-iRPE cells. Scale bar = 50 μm.

(E–I) Enriched peaks of CRX binding to the target genes and fold enrichment of CRX immunoprecipitation compared with IgG control, as determined by qRT-PCR. Data are mean ± SD, unpaired two-sided t-tests, n = 3.

(J–M) Enriched peaks of MITF-A and NR2E1 binding to the target gene lin7a and fold enrichment of MITF-A and NR2E1 immunoprecipitation compared with IgG control, as determined by qRT-PCR. Data are mean ± SD, unpaired two-sided t-tests, n = 3.

(N) Schematic model for the regulation of EMT and MET processes by the four TFs. CRX, MITF-A, NR2E1, and C-MYC directly or indirectly regulated the expression of *bmp7*, *lin7a*, pard6b, *ppm1a*, and *foxf2* to inhibit EMT and promote MET.

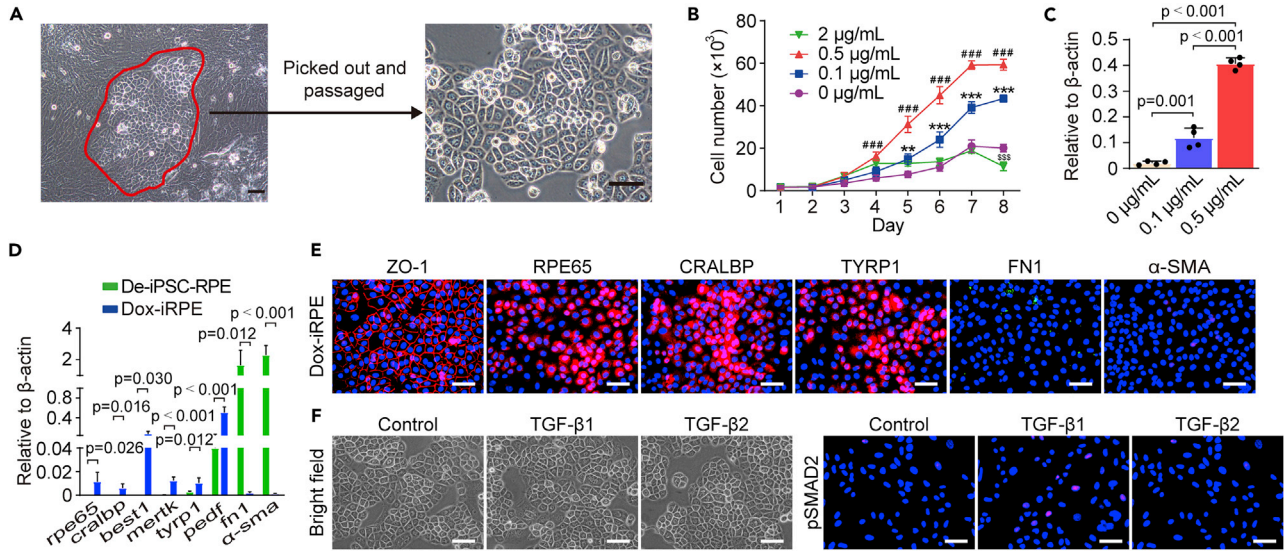

Figure 7. Generation of Dox-iRPE cells with Tet-on system-regulated *c-myc* expression

(A) Tet-on-C-MYC, MITF-A, CRX, and NR2E1 converted De-iPSC-RPE cells into iRPE (Dox-iRPE) cells. Scale bar = 50 μm.

(B) Cell proliferation ratio of Dox-iRPE cells treated with different Dox doses. Data are mean ± SD, one-way ANOVA and post hoc Bonferroni test, n = 4. ###p < 0.001, **p < 0.01, ***p < 0.001, $$$p < 0.001, compared with 0 μg Dox group.

(C) The expression level of *c-myc* in Dox-iRPE cells treated with different doses of Dox. Data are mean ± SD, one-way ANOVA and post hoc Bonferroni test, n = 4.

(D and E) qRT-PCR and immunostaining demonstrated that Dox-iRPE cells expressed RPE-specific markers. Scale bar = 50 μm. Data are mean ± SD, unpaired two-sided t-tests, n = 4.

(F) Morphology and pSMAD2 immunostaining of Dox-iRPE cells demonstrated that the cells were resistant to EMT induced by TGF-β1 or TGF-β2. Scale bar = 50 μm.

2020). A previous study reported that PPM1A could dephosphorylate and promote the nuclear export of TGF-β-activated SMAD2/3 (Lin et al., 2006). In the present study, knockdown of ppm1a resulted in EMT in iRPE cells, further confirming the anti-EMT function of PPM1A. Thus, employing a phosphatase to inhibit EMT in RPE cells may be a useful strategy for the treatment of AMD in the future.

Among the four key TFs identified, only CRX regulated the expression of all five factors (bmp7, foxf2, lin7a, pard6b, and ppm1a) directly or indirectly. Therefore, it plays a dominant role in inducing MET in De-iPSC-RPE cells. During retinal development, CRX is thought to be a key TF involved in photoreceptor cell fate determination (Furukawa et al., 1997). Mutations in human crx are associated with several retinal diseases, such as cone-rod dystrophy and Leber congenital amaurosis (Sohocki et al., 1998). Although CRX was not expressed in RPE cells, its overexpression in De-iPSC-RPE cells inhibited the expression of FOXF2 and induced the expression of BMP7, LIN7A, PARD6B, and PPM1A, thereby conferring EMT resistance to iRPE cells.

The *Mitf* encodes a TF belonging to the basic helix-loop-helix and leucine zipper family (Opdecamp et al., 1997). Ectopic expression of MITF in the quail neural retina induced a pigmented RPE phenotype (Planque et al., 2004), whereas knockout of *mitf* resulted in impairment of presumptive RPE development and partial conversion of the dorsal RPE to the neural retina (Nakayama et al., 1998; Nguyen and Arnheiter, 2000). MITF is expressed in multiple isoforms, and MITF-A, MITF-H, and MITF-D are dominant in RPE cells (Bharti et al., 2008). MITF-A plays a more important role in the EMT process in RPE cells (Liu et al., 2009); therefore, we selected MITF-A as a component of the TF cocktail to induce MET in De-iPSC-RPE cells.

NR2E1 is expressed in retinal progenitor cells (RPCs) and regulates retinal organization (Miyawaki et al., 2004). Downregulation of nr2e1 expression decreases RPC proliferation and accelerates neuronal and glial differentiation, whereas its upregulation enhances RPC proliferation (Ni et al., 2014). Our results showed that removing NR2E1 from the TF cocktail only marginally influenced the expression of RPE-specific genes but promoted the expression of LIN7A and BMP7. This suggests that NR2E1 does not regulate RPE-specific genes but functions in maintaining the iRPE cell epithelial phenotype.

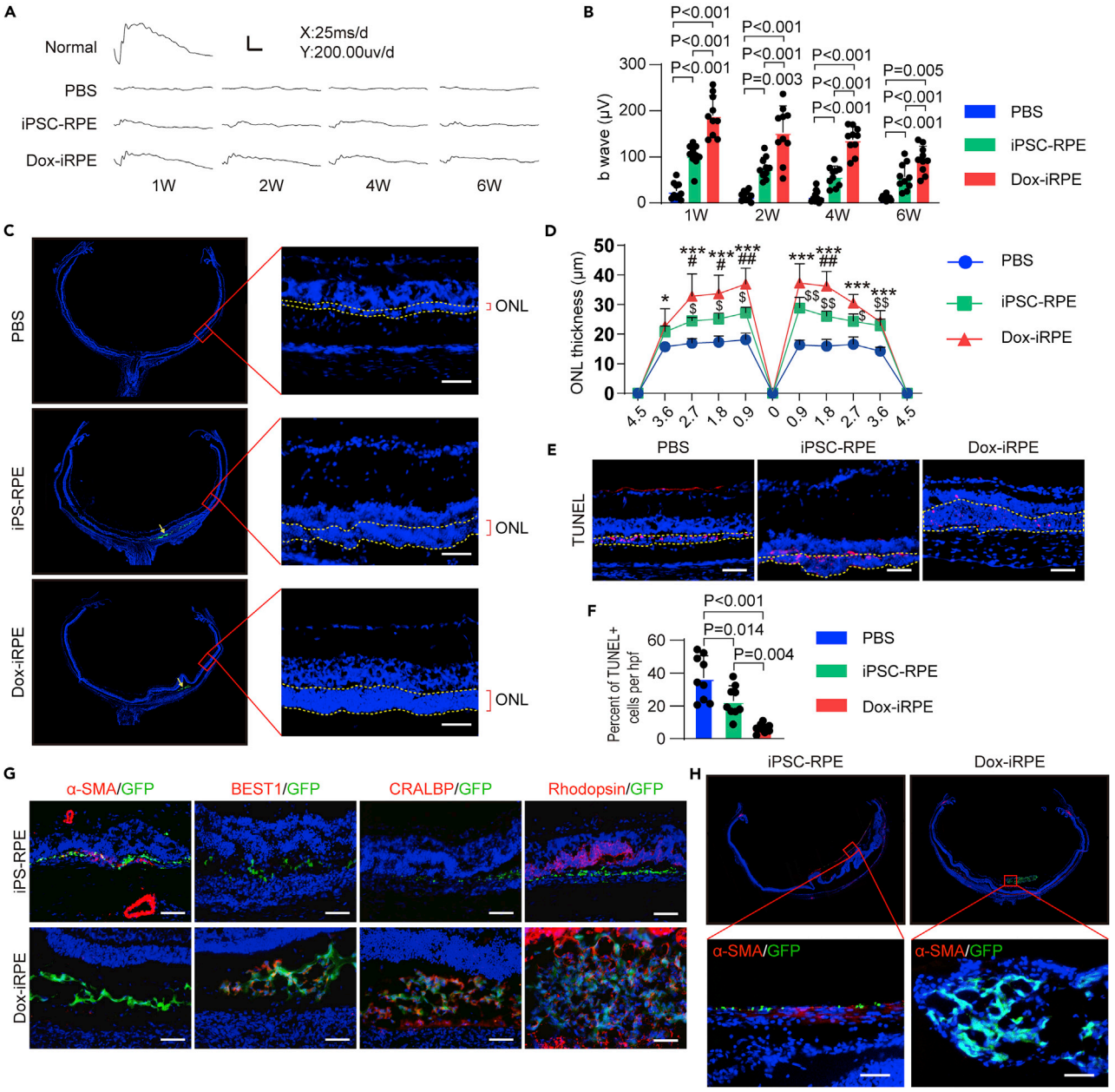

Figure 8. Dox-iRPE cells demonstrated anti-EMT capacity and delayed retinal degeneration in rat AMD model

(A) iPSC-RPE cells or Dox-iRPE cells were grafted into subretinal space of rat AMD model induced by sodium iodate. ERG waveforms recorded at different time points after transplantation of cells (the calibration indicates 200 μV vertically and 25 ms horizontally).

(B) Quantitative analysis of ERG b-wave amplitude. Data are mean ± SD, one-way ANOVA and post hoc Bonferroni test, n = 10.

(C and D) Representative micrographs of retinal samples at week 6 after transplantation (C) and Quantitative analysis of ONL thickness (D). iRPE cells demonstrated better retinal protective effect than iPSC-RPE and PBS groups. Arrow indicated the grafted GFP-labeled cells, ONL was between yellow dashed lines. Scale bar = 50 μm. Data are mean ± SD, one-way ANOVA and post hoc Bonferroni test, n = 9. *p < 0.05, ***p < 0.001, compared with PBS group; #p < 0.05, ##p < 0.01 compared with iPSC-RPE group; $p < 0.05, $$p < 0.01 compared with PBS group.

(E and F) Representative micrographs of retinal samples stained with TUNEL at week 6 after transplantation (E) and statistical analysis of the percentage of apoptotic cells in ONL (F). Less apoptotic photoreceptors were observed in iRPE group compared with iPSC-RPE and PBS groups. ONL was between yellow dashed lines. Scale bar = 50 μm. Data are mean ± SD, one-way ANOVA and post hoc Bonferroni test, n =9.

(G) Dox-iRPE cells, not iPSC-RPE cells, showed negative staining for α-SMA, and positive staining for RPE specific markers and Rhodopsin. Scale bar = 50 μm.

(H) Intravitreally grafted iPSC-RPE cells, not Dox-iRPE cells, formed an ERM-like structure and were positive staining for α-SMA. Scale bar = 50 μm.

C-MYC belongs to the MYC family of TFs. Generally, C-MYC is thought to play important roles in the control of cell proliferation, growth, differentiation, apoptosis, survival, stem cell self-renewal, and robust triggering of EMT in mammary epithelial cells (Cho et al., 2010; Cowling and Cole, 2007; Soucek and Evan, 2010). However, ectopic expression of human c-myc in the embryonic fibroblasts of Tibetan miniature pigs caused cells to undergo epithelial-like morphological changes through RhoA/Rock pathway inactivation (Shi et al., 2013). In the present study, we used a Tet-on system to regulate c-myc expression and generated Dox-iRPE cells. Even after removal of Dox, the cells maintained their epithelial phenotype and exhibited anti-EMT property. In addition, C-MYC did not directly regulate the expression of the key factors (*bmp7*, *foxf2*, *lin7a*, *pard6b*, and *ppm1a*), suggesting that C-MYC may only promote the efficient converting of De-iPSC-RPE cells into iRPE cells.

RPE cells can be transplanted into the subretinal space either in suspension or as a monolayer. Both approaches have been used in preclinical experiments and clinical trials (da Cruz et al., 2018; Davis et al., 2017; Liu et al., 2018; Liu et al., 2021; Mandai et al., 2017; Mehat et al., 2018; Schwartz et al., 2015; Song et al., 2015; Stanzel et al., 2014; Sugita et al., 2020; Sung et al., 2021; Takagi et al., 2019). Transplantation of human ESC-RPE cells or iPSC-RPE cells has several benefits in patients, such as ceasing CNV, recovering the activity of a few photoreceptors, inhibiting vessel leakage, and halting GA lesion expansion. Dr. Massayo Takahashi compared the two approaches by transplanting iPSC-RPE cell sheets or cell suspensions into the subretinal space of RCS rats and found no significant difference in terms of protection of visual functions (Kamao et al., 2014). Liu et al. transplanted human RPE stem cell-derived RPE cells under the macula of a non-human primate model for 3 months and did not observe the grafted cells undergoing EMT (Liu et al., 2021). Transplantation of iPSC-RPE cell sheets into the subretinal space of patients with AMD maintained the epithelial phenotype for a long time, thus confirming the advantage of cell sheet transplantation. However, the surgery used for grafting cell sheets into the subretinal space is more complex and has a higher risk of complications than the cell suspension delivery method. Usually, the cell sheet transplantation strategy can be used for patients with wet AMD with CNV that must be removed. When scar formation is not a serious complication in patients with long-term use of anti-VEGF antibodies, and CNV removal is not required, the cell suspensions may be better than RPE sheet. However, the disadvantage of cell suspension method is the risk of grafted cells leaking into vitreous cavity and forming ERM. Thus, iRPE cells with anti-EMT property may be more suitable for the treatment of such patients.

In summary, the four TFs (CRX, MITF-A, NR2E1, and C-MYC) successfully induced MET in dedifferentiated human iPSC-RPE cells to generate iRPE cells. The TF cocktail targeting *bmp7* and *foxf2* inhibited EMT in iRPE cells, maintained the epithelial polarity of iRPE cells by promoting the expression of *lin7a* and *pard6b*, and conferred resistance to TGF-β induction in iRPE cells by regulating the expression of *ppm1a*. iRPE cells with Tet-on system-regulated *c-myc* expression were found to be safe for *in vivo* transplantation, possessed EMT-resistant capacity and exhibited better therapeutic function than iPSC-RPE cells in rat AMD model. Thus, our study identified appropriate candidate cells for effective AMD treatment. This strategy of endowing cells with anti-EMT function may be used to treat other EMT-related diseases, such as pulmonary and renal fibrosis.

Limitations of the study

A limitation of this study is that we used retroviruses to integrate the four TFs into the chromosomes of De-iPSC-RPE cells to convert them into iRPE cells and continuous expression of the TFs to confer EMT resistance in iRPE cells. Although Dox-iRPE cells with Tet-on system-regulated *c-myc* expression were safe to a certain degree, the best method may be to integrate the key transcription factor genes into the AAVS1 (also known as PPP1R12C) locus, a well-validated "safe harbor" in the human genome (Sadelain et al., 2011), to avoid tumorigenicity or death caused by random integration. Furthermore, because most of the grafted cells died at week 6 after transplantation, an appropriate immunosuppressing scheme is required to prolong the survival of grafted cells in animal models.

STAR★METHODS

Detailed methods are provided in the online version of this paper and include the following:

- KEY RESOURCES TABLE
- RESOURCE AVAILABILITY
  - Lead contact
  - Materials availability
  - Data and code availability

SUPPLEMENTAL INFORMATION

Supplemental information can be found online at https://doi.org/10.1016/j.isci.2022.105050.

ACKNOWLEDGMENTS

This work was supported by grants obtained from the Ministry of Science and Technology of the People's Republic of China (2020YFA0113102 and 2017YFA0104100), National Natural Science Foundation of China (81770942 and 81670867).

AUTHOR CONTRIBUTIONS

Conceptualization, H.T., L.L., and G.T.X.; Methodology, H.T., Z.C., and X.Z.; Software, Z.W. and B.W.; Investigation, H.T., Z.C., X.Z., and Q.O.; Writing – Original Draft, H.T., Z.C., and X.Z.; Writing – Review and Editing, J.Y.X., C.J., F.G., J.W., J.Z., L.L., and G.T.X.; Funding Acquisition, H.T., L.L., and G.T.X.; Resources, Z.W. and B.W.; Supervision, H.T., L.L., and G.T.X.

DECLARATION OF INTERESTS

The authors declare no competing interests.

Received: April 26, 2022
Revised: July 12, 2022
Accepted: August 25, 2022
Published: October 21, 2022

REFERENCES

Alarcon, V.B. (2010). Cell polarity regulator PARD6B is essential for trophectoderm formation in the preimplantation mouse embryo. Biol. Reprod. *83*, 347–358.

Alexander, P., Thomson, H.A.J., Luff, A.J., and Lotery, A.J. (2015). Retinal pigment epithelium transplantation: concepts, challenges, and future prospects. Eye *29*, 992–1002.

Amin, R., Puklin, J.E., and Frank, R.N. (1994). Growth factor localization in choroidal neovascular membranes of age-related macular degeneration. Invest. Ophthalmol. Vis. Sci. *35*, 3178–3188.

Bazzoun, D., Lelièvre, S., and Talhouk, R. (2013). Polarity proteins as regulators of cell junction complexes: implications for breast cancer. Pharmacol. Ther. *138*, 418–427.

Bharti, K., Liu, W., Csermely, T., Bertuzzi, S., and Arnheiter, H. (2008). Alternative promoter use in eye development: the complex role and regulation of the transcription factor MITF. Development *135*, 1169–1178.

Binder, S., Stolba, U., Krebs, I., Kellner, L., Jahn, C., Feichtinger, H., Povelka, M., Frohner, U., Kruger, A., Hilgers, R.D., and Krugluger, W. (2002). Transplantation of autologous retinal pigment epithelium in eyes with foveal neovascularization resulting from age-related macular degeneration: a pilot study. Am. J. Ophthalmol. *133*, 215–225.

Chen, G., Gulbranson, D.R., Hou, Z., Bolin, J.M., Ruotti, V., Probasco, M.D., Smuga-Otto, K., Howden, S.E., Diol, N.R., Propson, N.E., et al. (2011). Chemically defined conditions for human iPSC derivation and culture. Nat. Methods *8*, 424–429.

Chen, X., Xiao, W., Liu, X., Zeng, M., Luo, L., Wu, M., Ye, S., and Liu, Y. (2014). Blockade of Jagged/Notch pathway abrogates transforming growth factor beta2-induced epithelial-mesenchymal transition in human retinal pigment epithelium cells. Curr. Mol. Med. *14*, 523–534.

Cho, K.B., Cho, M.K., Lee, W.Y., and Kang, K.W. (2010). Overexpression of c-myc induces epithelial mesenchymal transition in mammary epithelial cells. Cancer Lett. *293*, 230–239.

Cowling, V.H., and Cole, M.D. (2007). E-cadherin repression contributes to c-Myc-induced epithelial cell transformation. Oncogene *26*, 3582–3586.

Curran, S., Strandkvist, C., Bathmann, J., de Gennes, M., Kabla, A., Salbreux, G., and Baum, B. (2017). Myosin II controls junction fluctuations to Guide epithelial tissue ordering. Dev. Cell *43*, 480–492.e6.

da Cruz, L., Fynes, K., Georgiadis, O., Kerby, J., Luo, Y.H., Ahmado, A., Vernon, A., Daniels, J.T., Nommiste, B., Hasan, S.M., et al. (2018). Phase 1 clinical study of an embryonic stem cell-derived retinal pigment epithelium patch in age-related macular degeneration. Nat. Biotechnol. *36*, 328–337.

D'Alessio, A.C., Fan, Z.P., Wert, K.J., Baranov, P., Cohen, M.A., Saini, J.S., Cohick, E., Charniga, C., Dadon, D., Hannett, N.M., et al. (2015). A systematic approach to identify candidate transcription factors that control cell identity. Stem Cell Rep. *5*, 763–775.

Davis, R.J., Alam, N.M., Zhao, C., Müller, C., Saini, J.S., Blenkinsop, T.A., Mazzoni, F., Campbell, M., Borden, S.M., Charniga, C.J., et al. (2017). The developmental stage of adult human stem cell-derived retinal pigment epithelium cells influences transplant efficacy for vision rescue. Stem Cell Rep. *9*, 42–49.

Furukawa, T., Morrow, E.M., and Cepko, C.L. (1997). Crx, a novel otx-like homeobox gene, shows photoreceptor-specific expression and regulates photoreceptor differentiation. Cell *91*, 531–541.

Ghosh, S., Shang, P., Terasaki, H., Stepicheva, N., Hose, S., Yazdankhah, M., Weiss, J., Sakamoto, T., Bhutto, I.A., Xia, S., et al. (2018). A role for betaA3/A1-crystallin in type 2 EMT of RPE cells occurring in dry age-related macular degeneration. Invest. Ophthalmol. Vis. Sci. *59*, AMD104–AMD113.

Gruel, N., Fuhrmann, L., Lodillinsky, C., Benhamo, V., Mariani, O., Cédenot, A., Arnould, L., Macgrogan, G., Sastre-Garau, X., Chavrier, P., et al. (2016). LIN7A is a major determinant of cell-polarity defects in breast carcinomas. Breast Cancer Res. *18*, 23.

Grunwald, J.E., Daniel, E., Huang, J., Ying, G.S., Maguire, M.G., Toth, C.A., Jaffe, G.J., Fine, S.L., Blodi, B., Klein, M.L., et al. (2014). Risk of geographic atrophy in the comparison of age-related macular degeneration treatments trials. Ophthalmology *121*, 150–161.

Guan, Y., Cui, L., Qu, Z., Lu, L., Wang, F., Wu, Y., Zhang, J., Gao, F., Tian, H., Xu, L., et al. (2013). Subretinal transplantation of rat MSCs and erythropoietin gene modified rat MSCs for protecting and rescuing degenerative retina in rats. Curr. Mol. Med. *13*, 1419–1431.

Hadziahmetovic, M., and Malek, G. (2020). Age-related macular degeneration revisited: from pathology and cellular stress to potential therapies. Front. Cell Dev. Biol. *8*, 612812.

Hazim, R.A., Karumbayaram, S., Jiang, M., Dimashkie, A., Lopes, V.S., Li, D., Burgess, B.L., Vijayaraj, P., Alva-Ornelas, J.A., Zack, J.A., et al. (2017). Differentiation of RPE cells from integration-free iPS cells and their cell biological characterization. Stem Cell Res. Ther. *8*, 217.

Hirasawa, M., Noda, K., Noda, S., Suzuki, M., Ozawa, Y., Shinoda, K., Inoue, M., Ogawa, Y., Tsubota, K., and Ishida, S. (2011). Transcriptional factors associated with epithelial-mesenchymal transition in choroidal neovascularization. Mol. Vis. *17*, 1222–1230.

Hu, C., La, H., Wei, X., Zhou, Y., Ou, Q., Chen, Z., Zhu, X., Xu, J.Y., Jin, C., Gao, F., et al. (2020). Transplantation site affects the outcomes of adipose-derived stem cell-based therapy for retinal degeneration. Stem Cells Int. *2020*, 9625798.

Hussain, R.M., Dubovy, S.R., Kuriyan, A.E., Zhou, X.Y., Flynn, H.W., Jr., and Albini, T.A. (2019). Clinicopathologic correlations of retinal membranes associated with intravitreal 'stem cell' injections. Ophthalmic Surg. Lasers Imaging Retina *50*, 125–131.

Kamao, H., Mandai, M., Okamoto, S., Sakai, N., Suga, A., Sugita, S., Kiryu, J., and Takahashi, M. (2014). Characterization of human induced pluripotent stem cell-derived retinal pigment epithelium cell sheets aiming for clinical application. Stem Cell Rep. *2*, 205–218.

Kimura, K., Orita, T., Liu, Y., Yang, Y., Tokuda, K., Kurakazu, T., Noda, T., Yanai, R., Morishige, N., Takeda, A., et al. (2015). Attenuation of EMT in RPE cells and subretinal fibrosis by an RAR-gamma agonist. J. Mol. Med. *93*, 749–758.

Kuriyan, A.E., Albini, T.A., Townsend, J.H., Rodriguez, M., Pandya, H.K., Leonard, R.E., 2nd, Parrott, M.B., Rosenfeld, P.J., Flynn, H.W., Jr., and Goldberg, J.L. (2017). Vision loss after intravitreal injection of autologous "stem cells" for AMD. N. Engl. J. Med. *376*, 1047–1053.

Lin, X., Duan, X., Liang, Y.Y., Su, Y., Wrighton, K.H., Long, J., Hu, M., Davis, C.M., Wang, J., Brunicardi, F.C., et al. (2006). PPM1A functions as a Smad phosphatase to terminate TGFbeta signaling. Cell *125*, 915–928.

Liu, Y., Xu, H.W., Wang, L., Li, S.Y., Zhao, C.J., Hao, J., Li, Q.Y., Zhao, T.T., Wu, W., Wang, Y., et al. (2018). Human embryonic stem cell-derived retinal pigment epithelium transplants as a potential treatment for wet age-related macular degeneration. Cell Discov. *4*, 50.

Liu, Y., Ye, F., Li, Q., Tamiya, S., Darling, D.S., Kaplan, H.J., and Dean, D.C. (2009). Zeb1 represses Mitf and regulates pigment synthesis, cell proliferation, and epithelial morphology. Invest. Ophthalmol. Vis. Sci. *50*, 5080–5088.

Liu, Z., Parikh, B.H., Tan, Q.S.W., Wong, D.S.L., Ong, K.H., Yu, W., Seah, I., Holder, G.E., Hunziker, W., Tan, G.S.W., et al. (2021). Surgical transplantation of human RPE stem cell-derived RPE monolayers into non-human primates with immunosuppression. Stem Cell Rep. *16*, 237–251.

Lu, B., Wang, S., Girman, S., McGill, T., Ragaglia, V., and Lund, R. (2010). Human adult bone marrow-derived somatic cells rescue vision in a rodent model of retinal degeneration. Exp. Eye Res. *91*, 449–455.

Mandai, M., Watanabe, A., Kurimoto, Y., Hirami, Y., Morinaga, C., Daimon, T., Fujihara, M., Akimaru, H., Sakai, N., Shibata, Y., et al. (2017). Autologous induced stem-cell-derived retinal cells for macular degeneration. N. Engl. J. Med. *376*, 1038–1046.

Martin, E., Girardello, R., Dittmar, G., and Ludwig, A. (2021). New insights into the organization and regulation of the apical polarity network in mammalian epithelial cells. FEBS J. *288*, 7073–7095.

May-Simera, H.L., Wan, Q., Jha, B.S., Hartford, J., Khristov, V., Dejene, R., Chang, J., Patnaik, S., Lu, Q., Banerjee, P., et al. (2018). Primary cilium-mediated retinal pigment epithelium maturation is disrupted in ciliopathy patient cells. Cell Rep. *22*, 189–205.

Mehat, M.S., Sundaram, V., Ripamonti, C., Robson, A.G., Smith, A.J., Borooah, S., Robinson, M., Rosenthal, A.N., Innes, W., Weleber, R.G., et al. (2018). Transplantation of human embryonic stem cell-derived retinal pigment epithelial cells in macular degeneration. Ophthalmology *125*, 1765–1775.

Meyer-Schaller, N., Heck, C., Tiede, S., Yilmaz, M., and Christofori, G. (2018). Foxf2 plays a dual role during transforming growth factor beta-induced epithelial to mesenchymal transition by promoting apoptosis yet enabling cell junction dissolution and migration. Breast Cancer Res. *20*, 118.

Miyawaki, T., Uemura, A., Dezawa, M., Yu, R.T., Ide, C., Nishikawa, S., Honda, Y., Tanabe, Y., and Tanabe, T. (2004). Tlx, an orphan nuclear receptor, regulates cell numbers and astrocyte development in the developing retina. J. Neurosci. *24*, 8124–8134.

Nakagawa, M., Koyanagi, M., Tanabe, K., Takahashi, K., Ichisaka, T., Aoi, T., Okita, K., Mochiduki, Y., Takizawa, N., and Yamanaka, S. (2008). Generation of induced pluripotent stem

cells without Myc from mouse and human fibroblasts. Nat. Biotechnol. *26*, 101–106.

Nakayama, A., Nguyen, M.T., Chen, C.C., Opdecamp, K., Hodgkinson, C.A., and Arnheiter, H. (1998). Mutations in microphthalmia, the mouse homolog of the human deafness gene MITF, affect neuroepithelial and neural crest-derived melanocytes differently. Mech. Dev. *70*, 155–166.

Nassar, K., Grisanti, S., Tura, A., Lüke, J., Lüke, M., Soliman, M., and Grisanti, S. (2014). A TGF-beta receptor 1 inhibitor for prevention of proliferative vitreoretinopathy. Exp. Eye Res. *123*, 72–86.

Nesbit, C.E., Tersak, J.M., and Prochownik, E.V. (1999). MYC oncogenes and human neoplastic disease. Oncogene *18*, 3004–3016.

Nguyen, M., and Arnheiter, H. (2000). Signaling and transcriptional regulation in early mammalian eye development: a link between FGF and MITF. Development *127*, 3581–3591.

Ni, N., Zhang, D., Xie, Q., Chen, J., Wang, Z., Deng, Y., Wen, X., Zhu, M., Ji, J., Fan, X., et al. (2014). Effects of let-7b and TLX on the proliferation and differentiation of retinal progenitor cells in vitro. Sci. Rep. *4*, 6671.

Olsen, O., Funke, L., Long, J.F., Fukata, M., Kazuta, T., Trinidad, J.C., Moore, K.A., Misawa, H., Welling, P.A., Burlingame, A.L., et al. (2007). Renal defects associated with improper polarization of the CRB and DLG polarity complexes in MALS-3 knockout mice. J. Cell Biol. *179*, 151–164.

Opdecamp, K., Nakayama, A., Nguyen, M.T., Hodgkinson, C.A., Pavan, W.J., and Arnheiter, H. (1997). Melanocyte development in vivo and in neural crest cell cultures: crucial dependence on the Mitf basic-helix-loop-helix-zipper transcription factor. Development *124*, 2377–2386.

Peyman, G.A., Blinder, K.J., Paris, C.L., Alturki, W., Nelson, N.C., Jr., and Desai, U. (1991). A technique for retinal pigment epithelium transplantation for age-related macular degeneration secondary to extensive subfoveal scarring. Ophthalmic Surg. *22*, 102–108.

Planque, N., Raposo, G., Leconte, L., Anezo, O., Martin, P., and Saule, S. (2004). Microphthalmia transcription factor induces both retinal pigmented epithelium and neural crest melanocytes from neuroretina cells. J. Biol. Chem. *279*, 41911–41917.

Rak, D.J., Hardy, K.M., Jaffe, G.J., and McKay, B.S. (2006). Ca++-switch induction of RPE differentiation. Exp. Eye Res. *82*, 648–656.

Reddy, V.M., Zamora, R.L., and Kaplan, H.J. (1995). Distribution of growth factors in subfoveal neovascular membranes in age-related macular degeneration and presumed ocular histoplasmosis syndrome. Am. J. Ophthalmol. *120*, 291–301.

Rong, J., and Liu, S. (2011). Effect of all-trans retinoic acid on the barrier function in human retinal pigment epithelial cells. Biochem. Biophys. Res. Commun. *407*, 605–609.

Ruan, Y., Jiang, S., and Gericke, A. (2021). Age-related macular degeneration: role of oxidative stress and blood vessels. Int. J. Mol. Sci. *22*, 1296.

Sadelain, M., Papapetrou, E.P., and Bushman, F.D. (2011). Safe harbours for the integration of new DNA in the human genome. Nat. Rev. Cancer *12*, 51–58.

Schwartz, S.D., Regillo, C.D., Lam, B.L., Eliott, D., Rosenfeld, P.J., Gregori, N.Z., Hubschman, J.P., Davis, J.L., Heilwell, G., Spirn, M., et al. (2015). Human embryonic stem cell-derived retinal pigment epithelium in patients with age-related macular degeneration and Stargardt's macular dystrophy: follow-up of two open-label phase 1/2 studies. Lancet *385*, 509–516.

Shi, J.W., Liu, W., Zhang, T.T., Wang, S.C., Lin, X.L., Li, J., Jia, J.S., Sheng, H.F., Yao, Z.F., Zhao, W.T., et al. (2013). The enforced expression of c-Myc in pig fibroblasts triggers mesenchymal-epithelial transition (MET) via F-actin reorganization and RhoA/Rock pathway inactivation. Cell Cycle *12*, 1119–1127.

Shih, Y.H., Radeke, M.J., Radeke, C.M., and Coffey, P.J. (2017). Restoration of mesenchymal RPE by transcription factor-mediated reprogramming. Invest. Ophthalmol. Vis. Sci. *58*, 430–441.

Sohocki, M.M., Sullivan, L.S., Mintz-Hittner, H.A., Birch, D., Heckenlively, J.R., Freund, C.L., McInnes, R.R., and Daiger, S.P. (1998). A range of clinical phenotypes associated with mutations in CRX, a photoreceptor transcription-factor gene. Am. J. Hum. Genet. *63*, 1307–1315.

Song, W.K., Park, K.M., Kim, H.J., Lee, J.H., Choi, J., Chong, S.Y., Shim, S.H., Del Priore, L.V., and Lanza, R. (2015). Treatment of macular degeneration using embryonic stem cell-derived retinal pigment epithelium: preliminary results in Asian patients. Stem Cell Rep. *4*, 860–872.

Soucek, L., and Evan, G.I. (2010). The ups and downs of Myc biology. Curr. Opin. Genet. Dev. *20*, 91–95.

Stanzel, B.V., Liu, Z., Somboonthanakij, S., Wongsawad, W., Brinken, R., Eter, N., Corneo, B., Holz, F.G., Temple, S., Stern, J.H., and Blenkinsop, T.A. (2014). Human RPE stem cells grown into polarized RPE monolayers on a polyester matrix are maintained after grafting into rabbit subretinal space. Stem Cell Rep. *2*, 64–77.

Strauss, O. (2005). The retinal pigment epithelium in visual function. Physiol. Rev. *85*, 845–881.

Sugita, S., Mandai, M., Hirami, Y., Takagi, S., Maeda, T., Fujihara, M., Matsuzaki, M., Yamamoto, M., Iseki, K., Hayashi, N., et al. (2020). HLA-matched allogeneic iPS cells-derived RPE transplantation for macular degeneration. J. Clin. Med. *9*, 2217.

Sung, Y., Lee, M.J., Choi, J., Jung, S.Y., Chong, S.Y., Sung, J.H., Shim, S.H., and Song, W.K. (2021). Long-term safety and tolerability of subretinal transplantation of embryonic stem cell-derived retinal pigment epithelium in Asian Stargardt disease patients. Br. J. Ophthalmol. *105*, 829–837.

Takagi, S., Mandai, M., Gocho, K., Hirami, Y., Yamamoto, M., Fujihara, M., Sugita, S., Kurimoto, Y., and Takahashi, M. (2019). Evaluation of transplanted autologous induced pluripotent stem cell-derived retinal pigment epithelium in exudative age-related macular degeneration. Ophthalmol. Retina *3*, 850–859.

van Romunde, S.H.M., Polito, A., Bertazzi, L., Guerriero, M., and Pertile, G. (2015). Long-term results of full macular translocation for choroidal neovascularization in age-related macular degeneration. Ophthalmology *122*, 1366–1374.

Wang, K., Li, H., Sun, R., Liu, C., Luo, Y., Fu, S., and Ying, Y. (2019). Emerging roles of transforming growth factor beta signaling in wet age-related macular degeneration. Acta Biochim. Biophys. Sin. *51*, 1–8.

Wang, L., Li, P., Tian, Y., Li, Z., Lian, C., Ou, Q., Jin, C., Gao, F., Xu, J.Y., Wang, J., et al. (2017). Human umbilical cord mesenchymal stem cells: subpopulations and their difference in cell biology and effects on retinal degeneration in RCS rats. Curr. Mol. Med. *17*, 421–435.

Wang, S., Lu, B., Wood, P., and Lund, R.D. (2005). Grafting of ARPE-19 and Schwann cells to the subretinal space in RCS rats. Invest. Ophthalmol. Vis. Sci. *46*, 2552–2560.

Wei, X., Luo, Y., and Hyde, D.R. (2006). Molecular cloning of three zebrafish lin7 genes and their expression patterns in the retina. Exp. Eye Res. *82*, 122–131.

Yao, H., Ge, T., Zhang, Y., Li, M., Yang, S., Li, H., and Wang, F. (2019). BMP7 antagonizes proliferative vitreoretinopathy through retinal pigment epithelial fibrosis in vivo and in vitro. FASEB J *33*, 3212–3224.

Zhang, K., Liu, G.H., Yi, F., Montserrat, N., Hishida, T., Esteban, C.R., and Izpisua Belmonte, J.C. (2014). Direct conversion of human fibroblasts into retinal pigment epithelium-like cells by defined factors. Protein Cell *5*, 48–58.

Zhou, M., Geathers, J.S., Grillo, S.L., Weber, S.R., Wang, W., Zhao, Y., and Sundstrom, J.M. (2020). Role of epithelial-mesenchymal transition in retinal pigment epithelium dysfunction. Front. Cell Dev. Biol. *8*, 501.

Zhou, Q., Dai, J., Chen, T., Dada, L.A., Zhang, X., Zhang, W., DeCamp, M.M., Winn, R.A., Sznajder, J.I., and Zhou, G. (2017). Downregulation of PKCzeta/Pard3/Pard6b is responsible for lung adenocarcinoma cell EMT and invasion. Cell. Signal. *38*, 49–59.

Zihni, C., Vlassaks, E., Terry, S., Carlton, J., Leung, T.K.C., Olson, M., Pichaud, F., Balda, M.S., and Matter, K. (2017). An apical MRCK-driven morphogenetic pathway controls epithelial polarity. Nat. Cell Biol. *19*, 1049–1060.

STAR★METHODS

KEY RESOURCES TABLE

REAGENT or RESOURCE	SOURCE	IDENTIFIER
Antibodies		
OCT4	Proteintech	60242-1-Ig, RRID:AB_2881364
NANOG	Proteintech	14295-1-AP, RRID:AB_1607719
SOX2	Proteintech	11064-1-AP, RRID:AB_2195801
ZO-1	Proteintech	21773-1-AP, RRID:AB_10733242
FN1	Proteintech	66042-1-Ig, RRID:AB_11182385
LIN7A	Proteintech	25150-1-AP, RRID:AB_2879925
PARD6B	Proteintech	13996-1-AP, RRID:AB_2159779
PPM1A	Proteintech	12961-1-AP, RRID:AB_2169763
BEST1	Proteintech	21910-1-AP, RRID:AB_2878944
CRALBP	Proteintech	15356-1-AP, RRID:AB_2178530
MITF-A	Proteintech	13092-1-AP, RRID:AB_10597698
CRX	Proteintech	12047-1-AP, RRID:AB_2292128
C-MYC	Proteintech	10828-1-AP, RRID:AB_2148585
β-Actin	Proteintech	66009-1-Ig, RRID:AB_2687938
GAPDH	Proteintech	60004-1-Ig, RRID:AB_2107436
Goat anti-mouse IgG (H + L), HRP conjugate	Proteintech	SA00001-1, RRID:AB_2722565
Goat Anti-Rabbit IgG(H + L), HRP conjugate	Proteintech	SA00001-2, RRID:AB_2722564
RPE65	Novus Biologicals	NB100-355, RRID:AB_10002148
SSEA4	Abcam	ab16287, RRID:AB_778073
NR2E1	Abcam	ab109179, RRID:AB_10866097
TYRP1	Abcam	ab235447, N/A
MERTK	Abcam	ab52968, RRID:AB_2143584
Rhodopsin	Abcam	ab98887, RRID:AB_10696805
MYOSIN	Abcam	ab2480, RRID:AB_303094
α-SMA	Abcam	ab5694, RRID:AB_2223021
FOXF2	Abcam	ab54993, RRID:AB_2105608
SMAD2	Abcam	ab33875, RRID:AB_777976
pSMAD2	Abcam	ab53100, RRID:AB_874025
pSMAD3	Abcam	ab52903, RRID:AB_882596
Ki67	Abcam	ab92742, RRID:AB_10562976
Phalloidin-iFluor 555	Yeasen Biotech	40734ES75, N/A
Claudin19	Invitrogen	PA5-101526, RRID:AB_2850960
Goat anti-Mouse IgG (H + L) Secondary Antibody, Alexa Fluor Plus 488	Invitrogen	A32723, RRID:AB_2633275
Goat anti-Mouse IgG (H + L) Secondary Antibody, Alexa Fluor Plus 555	Invitrogen	A32727, RRID:AB_2633276
Goat anti-Rabbit IgG (H + L) Secondary Antibody, Alexa Fluor Plus 488	Invitrogen	A32731, RRID:AB_2633280
Donkey anti-Rabbit IgG (H + L) Secondary Antibody, Alexa Fluor Plus 555	Invitrogen	A32794, RRID:AB_2762834
FLAG	MBL International	M185-3L, RRID:AB_11123930

(*Continued on next page*)

Continued

REAGENT or RESOURCE	SOURCE	IDENTIFIER
Plasmids		
pCXLE-hSK	Addgene	#27078, RRID:Addgene_27078
pCXLE-hUL	Addgene	#27080, RRID:Addgene_27080
pCXLE-hOCT3/4-shp53-F	Addgene	#27077, RRID:Addgene_27077
pMXs-sox2	Addgene	#17218, N/A
pMXs-c-myc	Addgene	#17220, N/A
pMXs-klf4	Addgene	#17219, N/A
pMXs-gfp	Addgene	#74203, N/A
pCMV-VSVG	Addgene	#8454, RRID:Addgene_8454
gag/pol	Addgene	#14887, RRID:Addgene_14887
FUW-tetO-hMYC	Addgene	#20723, RRID:Addgene_20723
FUW-M2rtTA	Addgene	#20342, RRID:Addgene_20342
psPAX2	Addgene	#12260, RRID:Addgene_12260
pMD2.G	Addgene	#12259, RRID:Addgene_12259
Experimental models: Cell lines		
ARPE19 cells	ATCC	RRID: CVCL_0145
HELA cells	ATCC	RRID: CVCL_0030
HEK293FT cells	ATCC	RRID: CVCL_6911
Experimental models: Organisms/strains		
Female SD rats	Shanghai SLAC Laboratory Animal Co.,Ltd	Slac:SD
Female nude mice	Shanghai SLAC Laboratory Animal Co.,Ltd	BALB/cAnSlac-nu/nu
Deposited data		
Raw and analyzed RNA-seq data	This study	GSE174064
Raw and analyzed ChIP-seq data	This study	GSE174063
Software and algorithms		
ImageJ software	https://imagej.nih.gov/ij/	RRID:SCR_003073
MACS	https://pypi.org/project/MACS/1.4.2/	N/A
IGV software	https://software.broadinstitute.org/software/igv/2.8.x	RRID:SCR_011793
GraphPad Prism 9 software	GraphPad Prism 9 software	RRID:SCR_002798

RESOURCE AVAILABILITY

Lead contact

Further information and requests for resources and reagents should be directed to and will be fulfilled by the lead contact, Haibin Tian (tianhb@tongji.edu.cn).

Materials availability

All data generated or analyzed during this study are included in this article.

Data and code availability

- The raw data of ChIP-seq and RNA-seq have been deposited in the NCBI GEO under accession number GSE174063 and GSE174064.
- This paper does not report original code
- Any additional information required to reanalyze the data reported in this paper is available from the lead contact upon request.

EXPERIMENTAL MODEL AND SUBJECT DETAILS

Animals

Six-week-old female SD rats and six-week-old female nude mice were used in this study. All animal procedures were performed according to the institutional guidelines and the Guide for the Care and Use of Laboratory Animals issued by the NIH and the guidelines of the animal experimentation ethics committee of Tongji University (Approved NO. TJAA09620210), and in accordance with the Association for Research in Vision and Ophthalmology Statement for the use of Animals in Ophthalmic and Vision Research.

Cell lines

hUCMSC

The hUCMSCs (male) were obtained from the Eastern Union Stem Cell and Gene Engineering Co., Ltd. (Huzhou, China). Cells were cultured in DMEM/F12 (Thermo Fisher Scientific, Carlsbad, CA) containing 10% FBS (Applied StemCell, Milpitas, CA) at 37°C, 5% CO_2.

Generation of human iPSCs

Human iPSCs were generated according to published report with some modification (Chen et al., 2011). Briefly, 5×10^5 hUC-MSCs were electroporated with 3μg of each episomal plasmid, including pCXLE-hSK, pCXLE-hUL and pCXLE-hOCT3/4-shp53-F (expressing SOX2, KLF4, L-MYC, LIN28, OCT3/4 and p53-targeting shRNA, Addgene, Cambridge, MA) using the following conditions: 900μV, 500ms and 1 pulse. After electroporation, cells were reseeded on a Matrigel (BD Bioscience, San Jose)-coated cell culture dish and cultured in DMEM/F12 containing 10% FBS. Two days later, medium was changed into mTeSRTM1 medium (STEMCELL Technologies Inc., Vancouver, Canada) containing 0.25 mM Sodium butyrate (Sigma, St. Louis, MO). The iPSC colonies were picked out by cloning ring and subcultured in mTeSRTM1 medium.

Differentiation of iPSCs into RPE cells

Differentiation was conducted according to previous report with modification (Hazim et al., 2017). Briefly, once growing to confluency, iPSCs were cultured in differentiation medium containing DMEM/F12, 15% knockout serum replacement, 1% nonessential amino acids, 2 mM glutamine, 50 U/mL penicillin, 50 mg/mL streptomycin (all from Invitrogen, Carlsbad, CA), and 10 mM nicotinamide (Sigma) in 6-well culture dishes (Costar, Corning Inc., Corning, NY) pretreated with Poly (2-hydroxyethyl methacrylate) (Sigma). 20 ng/mL Activin A (PeproTech Inc, Rocky Hill, NJ) was supplemented during the third and fourth weeks. After 8 weeks in suspension, pigmented areas were isolated by a surgical blade no. 15 and 30–50 clusters were cultured in dishes precoated with Matrigel and cultured 6 weeks in differentiation medium. For subculture, iPSC-RPE cells were dissociated with 0.25% trypsin/0.53mM EDTA, and cultured in differentiation medium in dishes precoated with Matrigel. For EMT, cells were passaged and cultured in DMEM/F12 supplemented with 10% FBS.

ARPE19 cells and HELA cells

ARPE19 cells (ATCC, Research Triangle Park, NC) were cultured in DMEM/F12 containing 10% FBS, and HELA cells (ATCC) were cultured in RPMI-1640 (Invitrogen) plus 10% FBS.

METHOD DETAILS

Viral infection and iPRE cell screening

For generating retroviruses, human cDNAs of *pax6*, *rax*, *six6*, *nr2e1*, *otx2*, *lhx2*, *crx* and *mitf-a* were obtained by PCR amplification from iPSCs differentiated cultures-derived mRNA templates (obtained from iPSCs differentiating into RPE cultures from second to fourth weeks) and cloned into pMXs vectors (Addgene). pMXs-sox2, pMXs-c-myc, pMXs-klf4 and pMXs-gfp were bought from Addgene. Flag was cloned into corresponding vectors to produce pMXs-flag-mitf-a, pMXs-flag-crx, pMXs-flag-ne2e1, pMXs-flag-c-myc, pMXs-flag-foxf2 and pMXs-flag-ppm1a. The packaging plasmids are pCMV-VSVG and gag/pol (Addgene). For Dox-iRPE cells preparation, the vectors FUW-tetO-hMYC, FUW-M2rtTA and packaging plasmids psPAX2, pMD2.G were used (Addgene). HEK293FT cells were seeded at a density between $5.0–7.0\times10^4$ cells/cm^2 and transfected by Lipofectamine 2000 (Invitrogen) with each transcription-factor virus. Eight hours later, media were refreshed. Individual supernatants containing virus were harvested at 48h and 72 h post-transfection and filtered with 0.45μm PVDF membrane (Millipore, Boston). De-iPSC-RPE cells

were plated in 10-cm culture dishes at 100,000 cells per well. The next day, cells were infected with an equal ratio of a combination of viruses. After transfection for 7 days, colonies constituted by cells with polygonal morphology were observed in the cultures. Colonies were picked out by cloning ring (Sigma) and subcultured with DMEM/F12 supplemented with 10% FBS.

qRT-PCR

Total RNA was extracted and reverse transcription was performed using Primescript™ RT Master Mix kit (Takara, Shiga, Japan). qRT-PCR was performed in a Chromo4 instrument cycler (Bio-Rad, Hercules) using Superreal Premix plus kit (Tiangen Biotech, Beijing, China). PCR amplification was carried out with the following cycling parameters: denaturation at 95°C for 5 min, followed by 40 cycles of 95°C for 30 s, 60°C for 30 s. Primer sequences (Synthesized by Sangon Biotech Co., Ltd., Shanghai, China) were listed in Tables S1–S3.

Immunostaining

For immunofluorescence analysis, fixed cells, cryosections from eyes and matrigel containing transplanted cells in nude mice, were permeabilized with 0.25% Triton X-100 (Sigma) for 2 min, washed with PBS, and then blocked with 2% bovine serum albumin (BSA, Sigma) in PBS. The sections were incubated with the primary antibodies (1:200) against OCT4, NANOG, SOX2, ZO-1, FN1, LIN7A, PARD6B, CRALBP, BEST1, PPM1A, MITF-A, CRX and C-MYC (Proteintech, Rosemont, IL); against SSEA4, TYRP1, α-SMA, FOXF2, MYOSIN, *p*-SMAD2, *p*-SMAD3, NR2E1, Rhodopsin, and Ki67 (Abcam, Cambridge, UK); against RPE65 (Novus Biologicals, Centennial, CO), and against FLAG (1:1000, MBL International, Woburn, MD) overnight at 4°C. They were then washed three times with PBS, followed by incubation with the fluorescent secondary antibodies (1:1000, invirogen) overnight. F-actin was stained with phalloidin-iFluor 555 (Yeasen Biotech, Shanghai, China). 4,6 diamidino-2-phenylindole dihydrochloride (DAPI, Sigma) was used to indicate the nucleus. The samples were then examined by fluorescence microscope (Olympus IX73, Tokyo, Japan). Antibodies were listed in key resources table.

Western blotting

The cells were lysed by RIPA buffer containing protease and phosphatase inhibitor (Sigma). The protein extracts (20 μg per sample) were separated by 10% SDS-PAGE gels, and transferred onto polyvinylidene difluoride membranes (Millipore, Bedford, MA). After blocked with 3% BSA in PBS for 1 h, membranes were incubated with primary antibodies against RPE65 (1:1000), BEST1 (1:500), CRALBP (1:1000), TYRP1 (1:1000), FN1 (1:1000), α-SMA (1:2000), FOXF2 (1:1000), LIN7A (1:500), PARD6B (1:500), PPM1A (1:500), *p*-SMAD2 (1:500), SMAD2 (1:1000, Abcam), FLAG (1:2000), β-Actin (1:5000, Proteintech), Claudin19 (1:1000, Invitrogen), MERTK (1:1000, Abcam), GAPDH (1:3000, Proteintech) for 12hat 4°C, followed by incubation with corresponding secondary antibodies for 1hat room temperature. The blots were visualized with a chemiluminescence imaging system (Tanon 5200, Shanghai, China) and quantified with ImageJ software. Antibodies were listed in key resources table.

TEM

TEM was conducted according to published report with some modification (May-Simera et al., 2018). Briefly, Cell were seeded into the upper chamber of a 24-transwell plate (0.4 μm pore, BD Biosciences, San Diego, CA). One month later, cells were fixed in 2.5% glutaraldehyde-buffered solution at room temperature for 2h and rinsed with PBS. Cells were then treated with 1% ice-cold osmium tetroxide for 1h. After osmication, tissues were rinsed in PBS and processed through a battery of ethanol dehydration steps (50%, 70%, 85%, and 100% ethanol) for plastic embedding. The micrographs were obtained by an electron microscope (Hitachi, HT7800, Japan).

POS phagocytosis assay

Porcine eyes were obtained from abattoir and POSs were isolated and purified from porcine retinas as described previously (Hu et al., 2020). Purified POSs were labeled with NHS-LC-Biotin (Thermo Fisher Scientific, Newton Drive, Carlsbad) and resuspended in culture medium at a concentration of 5×10^7 POSs/mL. RPE cells were incubated with POSs at 37°C, 5% CO_2 in a humidified incubator for 4h. Non-phagocyted POSs were removed by washing three times with PBS. Cells were fixed by 4% paraformaldehyde (PFA, Sigma) in PBS and incubated with FITC-labeled or CY3-labeled avidin (Invitrogen) for 10min. ZO-1

immunostaining was used to show the boundary of cells. DAPI was used to label nuclei. The samples were then examined by fluorescence microscope (Olympus IX73).

TER analysis

3 × 104 cells were seeded into the upper chamber of a 24-transwell plate (0.4 μm pore, BD Biosciences) and cultured in RPE culture medium for iPSC-RPE cells or DMDM/F12 with 10% FBS for other cells. Eight days or one month later, TER was analyzed. Briefly, the 24-transwell plate was removed from the incubator and placed at room temperature for 30 min. TER values were measured by volt-ohm meter using an electrode (EVOM2; World precision Instruments, Sarasota, FL).

Permeability analysis

When the cells grew 100% confluence in the upper chamber of a 24-transwell plate (0.4 μm), 200μL culture medium containing 10 μg/mL horseradish peroxidase (Sigma) was added into the upper chamber. 30 min or 60 min later, 20μL medium was taken from the lower chamber, mixed with 150μL TMB chromogenic reaction solution (Sigma). The absorbance value (OD value) at the 450nm wavelength was measured.

RNA-seq analysis

RNA library pools of the cells were established following the protocols of the Illumina mRNA-seq with 50ng of RNA from iPSC-RPE cells, De-iPSC-RPE cells, iRPE cells, 4TFs−mitf-a-PRE cells, 4TFs−crx-PRE cells, 4TFs−nr2e1-RPE cells and 4TFs−c-myc-RPE cells, and experiments were performed in the MAJORBIO company (Shanghai, China). Filtering and quality control checks of the raw reads from RNA-seq had been done by FastQC. The clean reads were mapped to reference sequences using SOAP2 aligner. The gene expression levels were calculated using FPKM method (Fragments per kilobase of transcript per million fragments mapped). Log2 fold change (FC) of FPKM (iRPE cells)/FPKM (De-iPSC-RPE cells) was used to identify DEGs between iRPE cells and De-iPSC-RPE cells. Only those genes indicating $|log2FC| > 2$ and adjusted $p < 0.05$ were regarded as DEGs.

ChIP-seq analysis

ChIP assays were performed according to chromatin immunoprecipitation protocol (Cell Signaling Technology, Beverly, MA). Briefly, FLAG-MITF-A-iRPE cells, FLAG-CRX-iRPE cells, FLAG-NR2E1-iRPE cells and FLAG-C-MYC-iRPE cells were generated. Ten million cells were treated with 1% formaldehyde for 10min and unreacted formaldehyde was quenched with glycine for 5 min. The cells were collected by scraping and were lysed with lysate buffer, the nuclear pellet was digested by micrococcal nuclease. Immunoprecipitation was performed on the lysate with 2 μg of anti-FLAG antibody for 4h, and then with ChIP-grade protein G magnetic beads for 2h. Chromatin was eluted from antibody/protein G magenetic beads and purified using spin columns. The DNA fragments were then sequenced using the Illumina HiSeq X-ten platform (Shanghai Biotechnology Co., Shanghai, China). Sequencing raw reads were preprocessed by filtering out sequencing adapters, short-fragment reads and other low-quality reads. Bowtie (version 0.12.8) was then used to map the clean reads to the human hg19 reference genome. The binding peaks were identified by MACS (version 1.4.2) and visualized by IGV software (version 2.8.9).

ELISA

Quiescent De-iPSC-RPE cells, iRPE cells, shCont-iRPE cells, shBmp7-iRPE cells, FLAG-FOXF2-iRPE cells, "4TFs minus 1" RPE cells were cultured in DMEM/F12 for 24h. The supernatants were collected. BMP7 was quantified by human BMP7 ELISA kit (R&D Systems, Minneapolis, MN). iPSC-RPE cells, De-iPSC-RPE cells, and iRPE cells were cultured in 24-transwell plate for one month, the supernatants from upper and lower chambers of 24-transwell plate were collected. PEDF and VEGF were quantified by PEDF ELISA kit (Elabscience, Wuhan, China) and VEGF ELISA kit (Proteintech).

Anti-EMT analysis

iPSC-RPE cells ($1\times10^5/cm^2$) and iRPE cells ($1\times10^5/cm^2$) were seeded in 24-well culture plate treated with 10 ng/mL TGF-β1 or 10 ng/mL TGF-β2 (PeproTech, Cranbury, NJ). Cells were cultured for 8 days and fixed with 4% PFA and the corresponding RPE markers and EMT markers were analyzed by immunostaining. For pSMAD2 analysis, iPSC-RPE cells and iRPE cells were seeded in 24 or 6-well culture plate and cultured for 1 day and starved in DMEM/F12 containing 0.5% FBS for 24h. Cells were stimulated with 10 ng/mL TGF-β1

or 10 ng/mL TGF-β2 and fixed in 24-well culture plate for immunostaining after 1h treatment, or lysed in 6-well culture plate for Western blotting after 1, 2, 4 or 8 h treatment.

Target gene knockdown

Lentiviral pLVX-shRNA2-ZsGreen1 (Takara) vector were used to prepare lentiviruses. The packaging plasmids are psPAX2 and pMD2.G. The targeting sequences of the two shRNA for each *bmp7*, *lin7a*, *pard6b* or *ppm1a* were included in Table S4. HEK293FT cells were transfected with vectors. Individual supernatants containing virus were harvested at 48h and used to infect iRPE cells. The positively transfected cells were sorted by FACS based on ZsGreen expression. The reduced expression of target genes at transcript level was determined by qRT-PCR. We chose the most efficient shRNA out of the two to do next experiments.

Flow cytometry

iRPE cells transfected with shRNA were detached and dissociated into single cells with 0.25% trypsin/0.53 mM EDTA buffer, then resuspended in PBS containing 1% BSA. GFP + cells were sorted and collected on a FACS Aria II instrument using Cellquest software (BD Bioscience).

Co-IP

Flag-ppm1a was integrated into iRPE cells, and 5×10^6 cells were lysed by 200 μL IP lysis buffer (Beyotime, Shanghai, China) and incubated with 10 μL anti-FLAG affinity gel (Bimake, Houston, TX) at 4°C overnight. The gel was washed with PBST for three times and the binding proteins were eluted with protein loading buffer at 95°C for 5min. After centrifugation, the samples were collected and used for Western blotting.

Cell proliferation

Cell proliferation assay was performed following the protocol of CCK-8 assay kit (Abcam). In brief, Dox-iRPE cells were seeded in 96-well culture plates at a density of 1500 cells/well in DMEM/F12 containing 10%FBS and different dosages of Dox. At indicated time points, CCK-8 reagent was added to each well and incubated for 2 h at 37°C. Using a microplate reader, the optical absorbance was measured at 450 nm.

Cell transplantation

The six-week-old SD rats were intravenously injected with sodium iodate (SI, 50 mg/kg, Sigma) to induce AMD model, 6h later, rats were received iPSC-RPE or Dox-iRPE cell transplantation according to published report with some modification (Hu et al., 2020). Briefly, rats were anesthetized by 2% sodium pentobarbital. A channel was created by inserting a 30-gauge needle, behind the limbus, into vitreous chamber. A 33-gauge needle was inserted into the subretinal space of the central retina and 3 microliters of the cell suspensions (1×10^5 cells/μL) were injected. The eyes received a sham injection of PBS were used as control. All the rats received cyclosporin A for immunosuppression (210 mg/L in drinking water, Xinfu Pharmaceutical Co., Ltd., Jiangsu, China) two days before the transplantation until the end of the experiment (Lu et al., 2010). For the intravitreal transplantation, a 33-gauge needle was inserted into the vitreous chamber and 3 microliters of the GFP-labeled cell suspensions (1×10^5 cells/μL) were injected into vitreous chamber.

ERG examination

Following cell transplantation, ERG examination was performed at weeks 1, 2, 4 and 6 after cell transplantation with AVES-2000 electrophysiological apparatus (Kanghuaruiming S&T, Chongqing, China). Animals were prepared under dim red light following overnight dark adaptation. An intensity of 6.325e-2cd●s/m enabled the recording of photoreceptor response, the average amplitude of b-waves was used as a major parameter to reflect retinal visual function.

Retina structure assessment

The SD rats were sacrificed with an overdose of sodium pentobarbital at post-transplantation 6 weeks. The eyeballs were removed immediately and fixed in 4% PFA. The embedded tissues were sectioned (10μm thickness) along the vertical meridian of the eye. The samples collected at post-transplantation 6 weeks were used to assess the retinal degeneration. Nuclei in the sectioned tissue were counterstained with DAPI. The degree of retinal degeneration was assessed by the thicknesses (μm) of retinal ONL which were measured at 10 different points within both the nasal and temporal hemispheres. The EMT of iPSC-RPE cells and Dox-RPE cells were analyzed by immunostaining.

TUNEL assay

Eye samples were collected at week 6 post-transplantation. TUNEL assay was conducted with *In Situ* Cell Death Detection Kit (Roche, Diagnostics, Switzerland), according to the manufacturer's instructions. Nuclei were counterstained with DAPI. The apoptosis of ONL was assessed based on the counts of TUNEL+ cells per field.

Tumorigenesis

3×10^6 cells were embedded in 50μL of Matrigel and subcutaneously injected into back of six-week-old female nude mice using a 1mL syringe with a 28G needle. Animals were monitored for 2 weeks (HELA cell group) and 4 months (iPRE cell group and Dox-iPRE cell group). At the end of the experiments, mice were sacrificed and cell masses were picked out and fixed with 4% PFA for cryosection preparation. HELA cells were used as positive control.

QUANTIFICATION AND STATISTICAL ANALYSIS

All values are expressed as mean ± SD. Data were analyzed using GraphPad Prism 9 software. All statistical analyses were performed using unpaired two-sided t-tests or one-way ANOVA and post hoc Bonferroni's test, ANOVA, where appropriate, with a representation of at least three independent experiments. Statistical significance was set at $p < 0.05$.